tures of two repeats of spectrin suggest models of flexibility. Cell *98*, 523–535.

Holm, L., and Sander, C. (1994). The FSSP database of structurally aligned protein fold families. Nucleic Acids Res. *22*, 3600–3609.

Ishizaki, T., Morishima, Y., Okamoto, M., Furuyashiki, T., Kato, T., and Narumiya, S. (2001). Coordination of microtubules and the actin cytoskeleton by the Rho effector mDia1. Nat. Cell Biol. *3*, 8–14.

Jones, T.A., Zou, J.Y., Cowan, S.W., and Kjeldgaard, M. (1991). Improved methods for building protein models in electron-density maps and the location of errors in these models. Acta Crystallogr. A *47*, 110–119.

Kabsch, W. (1993). Automatic processing of rotation diffraction data from crystals of initially unknown symmetry and cell constants. J. Appl. Crystallogr. *26*, 795–800.

Kohno, H., Tanaka, K., Mino, A., Umikawa, M., Imamura, H., Fujiwara, T., Fujita, Y., Hotta, K., Qadota, H., Watanabe, T., et al. (1996). Bni1p implicated in cytoskeletal control is a putative target of Rho1p small GTP binding protein in *Saccharomyces cerevisiae*. EMBO J. *15*, 6060–6068.

Koradi, R., Billeter, M., and Wüthrich, K. (1996). MOLMOL: a program for display and analysis of macromolecular structures. J. Mol. Graph. *14*, 51–55.

Kovar, D.R., Kuhn, J.R., Tichy, A.L., and Pollard, T.D. (2003). The fission yeast cytokinesis formin Cdc12p is a barbed end actin filament capping protein gated by profilin. J. Cell Biol. *161*, 875–887.

Kraulis, P.J. (1991). MolScript—a program to produce both detailed and schematic plots of protein structures. J. Appl. Crystallogr. *24*, 946–950.

Kurzawa, S.E., and Geeves, M.A. (1996). A novel stopped-flow method for measuring the affinity of actin for myosin head fragments using microgram quantities of protein. J. Muscle Res. Cell Motil. *17*, 669–676.

Li, F., and Higgs, H.N. (2003). The mouse formin mDia1 is a potent actin nucleation factor regulated by autoinhibition. Curr. Biol. *13*, 1335–1340.

Merrit, E.A., and Murphy, M.E.P. (1994). Raster3D version 2.0—a program for photorealistic molecular graphics. Acta Crystallogr. D *50*, 869–873.

Otwinowski, Z., and Minor, W. (1997). Processing of X-ray diffraction data collected in oscillation mode. Acta Crystallogr. A *276*, 307–326.

Palazzo, A.F., Cook, T.A., Alberts, A.S., and Gundersen, G.G. (2001). mDia mediates Rho-regulated formation and orientation of stable microtubules. Nat. Cell Biol. *3*, 723–729.

Posern, G., Sotiropoulos, A., and Treisman, R. (2002). Mutant actins demonstrate a role for unpolymerized actin in control of transcription by serum response factor. Mol. Biol. Cell *13*, 4167–4178.

Pring, M., Evangelista, M., Boone, C., Yang, C., and Zigmond, S.H. (2003). Mechanism of formin-induced nucleation of actin filaments. Biochemistry *42*, 486–496.

Pruyne, D., Evangelista, M., Yang, C., Bi, E., Zigmond, S., Bretscher, A., and Boone, C. (2002). Role of formins in actin assembly: nucleation and barbed-end association. Science *297*, 612–615.

Sagot, I., Klee, S.K., and Pellman, D. (2002a). Yeast formins regulate cell polarity by controlling the assembly of actin cables. Nat. Cell Biol. *4*, 42–50.

Sagot, I., Rodal, A.A., Moseley, J., Goode, B.L., and Pellman, D. (2002b). An actin nucleation mechanism mediated by Bni1 and Profilin. Nat. Cell Biol. *4*, 626–631.

Sotiropoulos, A., Gineitis, D., Copeland, J., and Treisman, R. (1999). Signal-regulated activation of serum response factor is mediated by changes in actin dynamics. Cell *98*, 159–169.

Spudich, J.A., and Watt, S. (1971). The regulation of rabbit skeletal muscle contraction. I. Biochemical studies of the interaction of the tropomyosin-troponin complex with actin and the proteolytic fragments of myosin. J. Biol. Chem. *246*, 4866–4871.

Stemlicht, H., and Ringel, I. (1979). Colchicine inhibition of microtubule assembly via copolymer formation. J. Biol. Chem. *254*, 10540–10550.

Takeya, R., and Sumimoto, H. (2003). Fhos, a mammalian formin, directly binds to F-actin via a region N-terminal to the FH1 domain and forms a homotypic complex via the FH2 domain to promote actin fiber formation. J. Cell Sci. *116*, 4567–4575.

Terwilliger, T.C., and Berendzen, J. (1996). Bayesian difference refinement. Acta Crystallogr. D *52*, 1004–1011.

Usón, I., and Sheldrick, G.M. (1999). Advances in direct methods for protein crystallography. Curr. Opin. Struct. Biol. *9*, 643–648.

Wallar, B.J., and Alberts, A.S. (2003). The formins: active scaffolds that remodel the cytoskeleton. Trends Cell Biol. *13*, 435–446.

Watanabe, N., Kato, T., Fujita, A., Ishizaki, T., and Narumiya, S. (1999). Cooperation between mDia1 and ROCK in Rho-induced actin reorganization. Nat. Cell Biol. *1*, 136–143.

Watanabe, N., Madaule, P., Reid, T., Ishizaki, T., Watanabe, G., Kakizuka, A., Saito, Y., Nakao, K., Jockusch, B.M., and Narumiya, S. (1997). p140mDia, a mammalian homolog of Drosophila diaphanous, is a target protein for Rho small GTPase and is a ligand for profilin. EMBO J. *16*, 3044–3056.

Wear, M.A., Yamashita, A., Kim, K., Maéda, Y., and Cooper, J.A. (2003). How capping protein binds the barbed end of the actin filament. Curr. Biol. *13*, 1531–1537.

Weeks, C.M., and Miller, R. (1999). Optimizing Shake-and-Bake for proteins. Acta Crystallogr. D *55*, 492–500.

Zigmond, S.H., Evangelista, M., Boone, C., Yang, C., Dar, A.C., Sicheri, F., Forkey, J., and Pring, M. (2003). Formin leaky cap allows elongation in the presence of tight capping proteins. Curr. Biol. *13*, 1820–1823.

Accession Numbers

The coordinates for the core FH2 domain of mDia1 have been deposited in the Protein Data Bank under ID code 1V9D.

Actin Polymerization–Driven Molecular Movement of mDia1 in Living Cells

Chiharu Higashida,[1] Takushi Miyoshi,[1] Akiko Fujita,[1] Fabian Oceguera-Yanez,[1] James Monypenny,[1] Yoshikazu Andou,[1] Shuh Narumiya,[1] Naoki Watanabe[1,2]*

mDia1, a Rho effector, belongs to the Formin family of proteins, which shares the conserved tandem FH1-FH2 unit structure. Formins including mDia1 accelerate actin nucleation while interacting with actin filament fast-growing ends. Here our single-molecule imaging revealed fast directional movement of mDia1 FH1-FH2 for tens of microns in living cells. The movement of mDia1 FH1-FH2 was blocked by actin-perturbing drugs, and the speed of mDia1 FH1-FH2 movement appeared to correlate with actin elongation rates. In vitro, mDia1 FH1-FH2 associated persistently with the growing actin barbed end. mDia1 probably moves processively along the growing end of actin filaments in cells, and Formins may be a molecular motility machinery that is independent from motor proteins.

Formin homology proteins (Formins) play essential roles in the regulation of specific actin-based structures (*1*, *2*), e.g., the contractile ring in cytokinesis (*3*, *4*); actin cables in budding yeasts (*5*–*7*); and actin fibers in animal cells (*8*). The structure of Formins is conserved in most of the C-terminal half including the FH1 and FH2 domains. The FH1 domain consists of poly-proline repeats that bind to profilin, and it is followed by conserved sequences of ~400 amino acids including the FH2 domain. This structural feature unique to Formins, called the FH1-FH2 unit (FH1-FH2) (*8*), implies a certain evolutionarily conserved function of FH1-FH2.

Yeast Formins (*9*–*12*) and mDia1 (*13*) have an actin nucleation-promoting activity in their FH1-FH2 or FH2 fragments. Nucleated actin filaments elongate at the fast-growing, barbed end. Formins have thus emerged as potential cellular actin nucleators. However, in marked contrast to the Arp2/3 complex, another actin nucleator, Formins bind the barbed end of actin filaments. Two models for how Formins allow barbed end elongation while binding the same site have been proposed. One is the profilin-gated mechanism for the barbed end capping by *Schizosaccharomyces pombe* Cdc12p (*12*). Alternatively, Bni1p and mDia1 function as "a leaky cap," and it has been postulated that Bni1p might "walk" along the barbed end of an elongating filament (*11*, *14*).

To explore the biochemical properties of Formins in living cells, we took an approach similar to single-molecule actin speckle analysis (*15*). We expressed mDia1 mutants fused to an enhanced green fluorescent protein (EGFP) (Fig. 1A) in XTC fibroblasts and carried out live-cell imaging of mDia1 expressed at a low level (*16*). mDia1ΔN3, an FH1-FH2 mutant, induced the formation of massive thin actin fibers, reminiscent of Rho-induced actin stress fibers (Fig. 1B) (*8*). Speckle microscopy revealed fast, directional molecular movement of EGFP-mDia1ΔN3 (Fig. 1C, Movie S1). Fluorescence intensity of moving signals was comparable to that of single-molecule EGFP-actin (*15*), which indicated that they consisted of single EGFP or a few EGFP molecules coupled to multimeric mDia1 (*13*). mDia1ΔN3 movement persisted along a long path that often spanned the radius of the cell (from the center to the edge). mDia1ΔN3 speckles could be tracked along a line or a wide arc, which suggests an association with certain cytoskeletal filaments. At the cell periphery, the majority of mDia1ΔN3 speckles moved outward along filopodium-like protrusions, accumulating in the tip region (Fig. 1B, inset; Movie S1). We also observed movement of mDia1F2 speckles. mDia1F2 is a mutant that is defective in promoting actin fiber formation (Fig. 1B) (*8*), and it weakly activates serum response factor (*17*). mDia1F2 speckles displayed slower rates of movement and traveled over shorter distances (Fig. 1D, Movie S2). The average speed of mDia1ΔN3 and mDia1F2 movement was 2.0 μm/s and 0.13 μm/s, respectively (Fig. 1E). The speed of mDia1ΔN3 movement is two orders of magnitude faster than the flow rate of the actin network (typically ~0.025 μm/s in lamellipodia of XTC cells) (*15*).

Unlike mDia1ΔN3 and mDia1F2, an EGFP-fusion of full-length mDia1, mDia1Full hardly exhibited any fast directional movement (Fig. 1F, left; Movie S3, top). We then tested whether administration of Rho affects the mobility of mDia1Full, as Rho binding to the mDia1 N terminus has been postulated to disrupt the autoinhibitory intramolecular interaction of mDia1, by exposing FH1-FH2 and thus permitting its

[1]Department of Pharmacology, Kyoto University Faculty of Medicine, Yoshida Konoe-cho, Sakyo-ku, Kyoto, Japan. [2]PRESTO, Japan Science and Technology Agency, 4-1-8 Honcho Kawaguchi, Saitama, Japan.

*To whom correspondence should be addressed. E-mail: naoki-w@mfour.med.kyoto-u.ac.jp

7 October 2003; accepted 26 January 2004

activity on actin (*8*, *13*, *18*). As early as 2 min after microinjection of recombinant RhoA-V14 (a constitutively active mutant), we frequently observed directional movement of mDia1Full similar to that of mDia1ΔN3 (Fig. 1F, right; Movie S3, bottom). The average speed of mDia1Full movement was 0.97 μm/s after microinjection. These results support a role for Rho binding in the molecular activation of mDia1 (*8*) within cells and demonstrate spatial and temporal molecular dynamics mediating a signal between Rho and actin reorganization (*19*).

We next examined which cytoskeletal filaments are required for mDia1 movement. Treatment of cells with 10 μM nocodazole depolymerized most microtubules, whereas mDia1ΔN3 movement was unchanged even in the area devoid of microtubules (Fig. 2A, Movie S4). In contrast, three actin-perturbing drugs, cytochalasin D (CD), latrunculin B (LatB), and jasplakinolide (Jas), decelerated and finally stopped mDia1ΔN3 movement completely (Fig. 2B, Movie S5, Fig. 3). Thus, the fast movement of mDia1 depended on the integrity or dynamics of actin filaments, but not of microtubules.

We next found evidence of an actin polymerization–driven mechanism that did not involve myosin facilitating the fast mDia1 movement. The three actin-perturbing drugs, CD, LatB, and Jas, attenuated EGFP-mDia1ΔN3 movement, but careful measurement revealed two types of change in the speed of individual mDia1ΔN3 speckles. A gradual deceleration was observed in cells treated with LatB (Fig. 3A, Movie S6) or with Jas (Fig. 3B, Movie S7), whereas sudden stoppage, which occurred within two consecutive images, was observed in CD-treated cells (Fig. 3C, Movie S8). The speckle stoppage occurred at various times and places in cells after CD treatment, and before arrest, speckles continued to move as fast as they did before drug administration. This clearly differed from the synchronous, gradual deceleration of all speckle movement after LatB or Jas treatment.

These changes in the speed of mDia1ΔN3 speckles correspond well to the predictable actin elongation rate change. Latrunculins bind actin monomers and decrease polymerization-competent monomers (*20*). For the other drugs, actin filament turnover, the $t_{1/2}$ of which is ~30 s (*15*), must be taken into consideration. Jas inhibits actin depolymerization (*21*), which would result in a gradual loss of monomers. CD binds the barbed end and inhibits filament elongation directly (*22*). Because the actin elongation rate is nearly proportional to the sum of the free monomer and profilin-actin concentrations (*23*), LatB or Jas treatment would decrease the elongation rate, whereas CD treatment would not decrease the elongation rate until it blocked barbed end growth. All of the speckle speed data (Fig. 3) fit with this estimated elongation rate change. Synchronous speckle deceleration in LatB- or Jas-treated cells might reflect gradual retardation of actin elongation as a consequence of actin monomer depletion. In CD-treated cells, mDia1ΔN3 speckles stopped suddenly, presumably when CD bound the barbed end, which occurred stochastically at different filaments. CD treatment did not abolish the association of mDia1ΔN3 with actin structures. Thus, the speed of mDia1ΔN3 movement is defined by the actin elongation rate in cells. Myosin involvement is unlikely, because actin filaments remained for the observed duration; also, the flow and con-

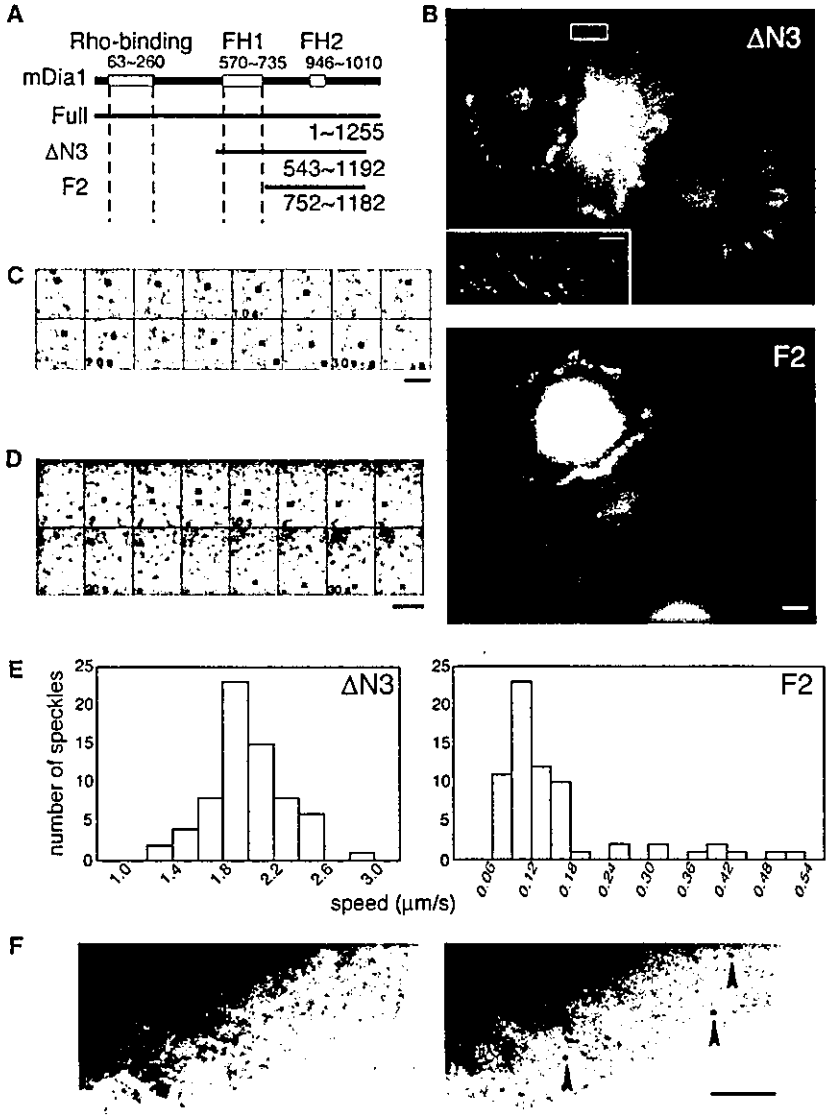

Fig. 1. Fast movement of EGFP-mDia1 mutants as revealed by single-molecule observations in living XTC cells. (A) Structures of mDia1 mutants. (B) Massive actin fibers observed in cells expressing EGFP-mDia1ΔN3 (top), but not in cells expressing EGFP-mDia1F2 (bottom). Actin filaments (red) and EGFP signals (green) are shown. Scale bar, 10 μm. Note the faint accumulation of EGFP-mDia1ΔN3 at the tip of filopodium-like processes (inset, scale bar, 2 μm). (C and D) Representative time-lapse images of mDia1ΔN3 (C) and mDia1F2 (D) speckles. Images of EGFP-mDia1 mutants expressed at a very low density were acquired. Each colored square indicates the same speckle followed over time. Scale bars, 5 μm. (E) Distribution of the speed of mDia1ΔN3 (left) and mDia1F2 (right) speckles. The speeds of mDia1ΔN3 and F2 movement (means ± SD) were 2.0 ± 0.30 μm/s, n = 67, three cells, and 0.13 ± 0.10 μm/s, n = 67, four cells, respectively. (F) Fast molecular movement of mDia1Full induced by RhoA-V14 microinjection. Time-lapse images of EGFP-mDia1Full were taken before (left) and 2 min after (right) RhoA-V14 microinjection. Arrowheads indicate mDia1Full, which emerged as a fast-moving speckle. Scale bar, 5 μm.

traction of the actin network, perhaps myosin-driven events, were not blocked by CD, LatB, or Jas. Taken together with the proposed biochemical property of a leaky cap of FH1-FH2 (*11*, *13*, *14*), our data suggest that mDia1 FH1-FH2 processively associates with the growing barbed end of actin filaments in cells.

In order to obtain direct evidence that mDia1 can move by a mechanism other than myosin, we reconstituted mDia1-catalyzed actin assembly using purified components and observed filament elongation relative to mDia1 FH1-FH2 under the microscope (*16*). We labeled recombinant glutathione *S*-transferase mDia1ΔN3 fused to (GST-mDia1ΔN3), using antibodies, which resulted in the formation of large protein aggregates containing GST-mDia1ΔN3. After actin and profilin were mixed with the labeling mixture, we observed marked outgrowth of actin filaments emanating from mDia1ΔN3-containing aggregates (Fig. 4, A to D; Movie S9). Speckle labeling of the filaments revealed the filament growth occurring at the aggregates but not at the distant end of the filaments (Fig. 4, E and F; Movies S10 and S11). We also observed growth of a single isolated filament from small mDia1ΔN3-containing aggregates (Fig. 4, G and H; Movie S12), which demonstrated continuous anchoring of the growing filament end to mDia1ΔN3. Filament growth at the rate of 0.040 μm/s (Fig. 4F) can occur only at the barbed end under these conditions. Thus, mDia1ΔN3 is capable of persistently binding the growing barbed end. This finding provides further evidence for myosin-independent movement of mDia1 FH1-FH2.

From our finding of long-distance mDia1 FH1-FH2 movement clinging to the growing barbed end of actin filaments, we may infer several possible roles of Formins. Their role may be to protect barbed ends from capping proteins (*14*). mDia1 FH1-FH2 frequently moved over a distance of >10 μm, although barbed end capping by capping proteins is estimated to occur within less than 1 s (*24*, *25*). In cooperation with profilin (*26*), Formins may play a role in generating long actin filaments, which may be a prerequisite for assembling actin stress fibers, cables, and the contractile ring.

Another possible role may be to accelerate barbed end growth. The speed of mDia1ΔN3 in cells, 2.0 μm/s, corresponds to the actin elongation rate by ~70 μM profilin-actin complex. This value seems slightly higher than a cellular profilin concentration, ~30 μM (*27*). However,

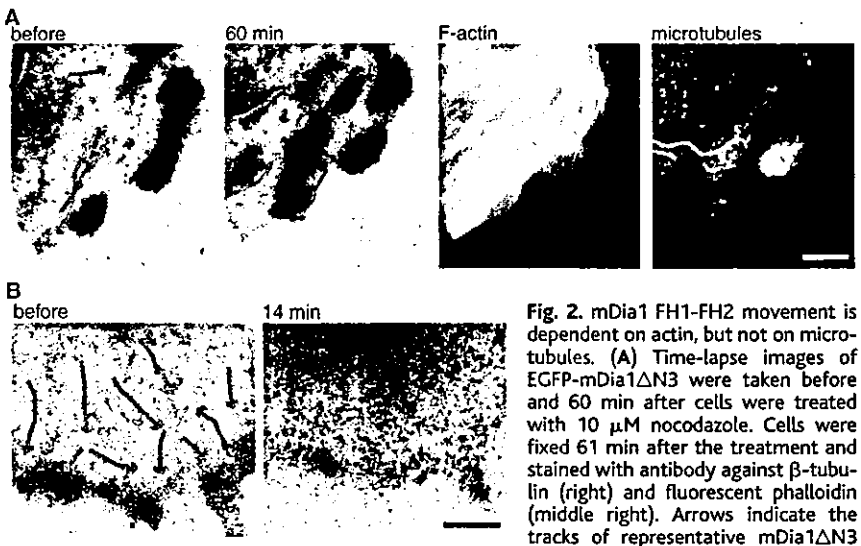

Fig. 2. mDia1 FH1-FH2 movement is dependent on actin, but not on microtubules. (**A**) Time-lapse images of EGFP-mDia1ΔN3 were taken before and 60 min after cells were treated with 10 μM nocodazole. Cells were fixed 61 min after the treatment and stained with antibody against β-tubulin (right) and fluorescent phalloidin (middle right). Arrows indicate the tracks of representative mDia1ΔN3 speckles. Speckles continued to move in an area devoid of microtubules after the treatment. The average speed of mDia1ΔN3 movement before and 60 min after the treatment was 1.1 μm/s, n = 15, and 1.0 μm/s, n = 15, respectively. (**B**) Arrows indicate the track of representative mDia1ΔN3 speckles (left). Speckle movement was not observed 14 min after 1 μM Jas treatment (right). Scale bars, 5 μm.

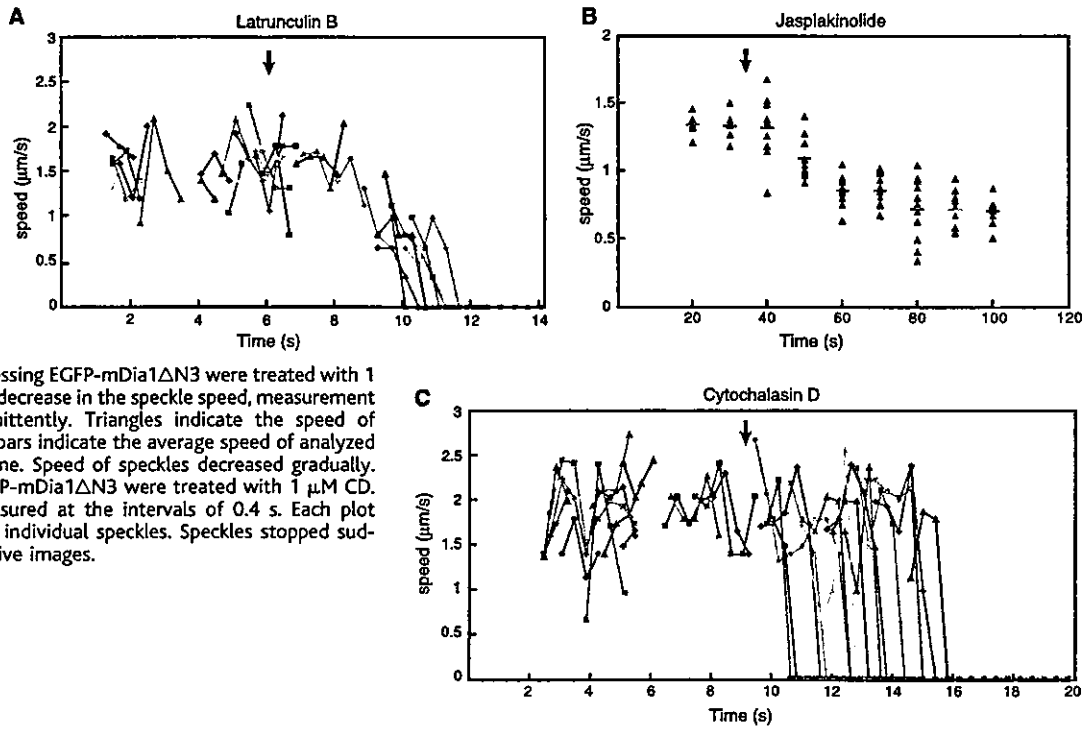

Fig. 3. Two types of mDia1ΔN3 speckle deceleration after treatment with three actin-perturbing drugs. (**A**) Cells expressing EGFP-mDia1ΔN3 were treated with 1 μM LatB. Each plot represents the speed of individual speckles measured at the intervals of 0.4 s. Speed of speckles decreased gradually and synchronously. Arrow shows the beginning of perfusion. (**B**) Cells expressing EGFP-mDia1ΔN3 were treated with 1 μM Jas. Due to the slow decrease in the speckle speed, measurement was carried out intermittently. Triangles indicate the speed of individual speckles, and bars indicate the average speed of analyzed speckles at indicated time. Speed of speckles decreased gradually. (**C**) Cells expressing EGFP-mDia1ΔN3 were treated with 1 μM CD. Speckle speed was measured at the intervals of 0.4 s. Each plot represents the speed of individual speckles. Speckles stopped suddenly within 2 consecutive images.

any acceleration of barbed end growth has not been detected so far (*13*).

The third possible role is to anchor the barbed end while allowing actin monomer exchange. In budding yeasts, live imaging of GFP-Abp140 detected fast extension of actin cables away from the bud (*28*), implying pointed end–directed actin translocation supported by certain barbed end factors. In animal cells, actin filaments do not freely move because of cross-linking, as proven by the constant relative position between actin speckles (*15*). Therefore, the anchoring mechanism, if it applies, might locally hold a cluster of growing filaments such as Rho-dependent actin fibers found at the *Shigella* entry into epithelial cells (*29*).

Finally, FH1-FH2 has the potential to act in cells as a motor driven by actin polymerization. The directional movement of mDia1 over tens of microns is a property known only for motor proteins. Actin polymerization has been regarded as a "motor" because it converts chemical energy to mechanical energy to drive cell edge protrusion (*30*). mDia1 can elicit such actin polymerization–driven motion at the molecular level, which raises the possibility that Formins comprise a molecular motility machinery fueled by actin polymerization.

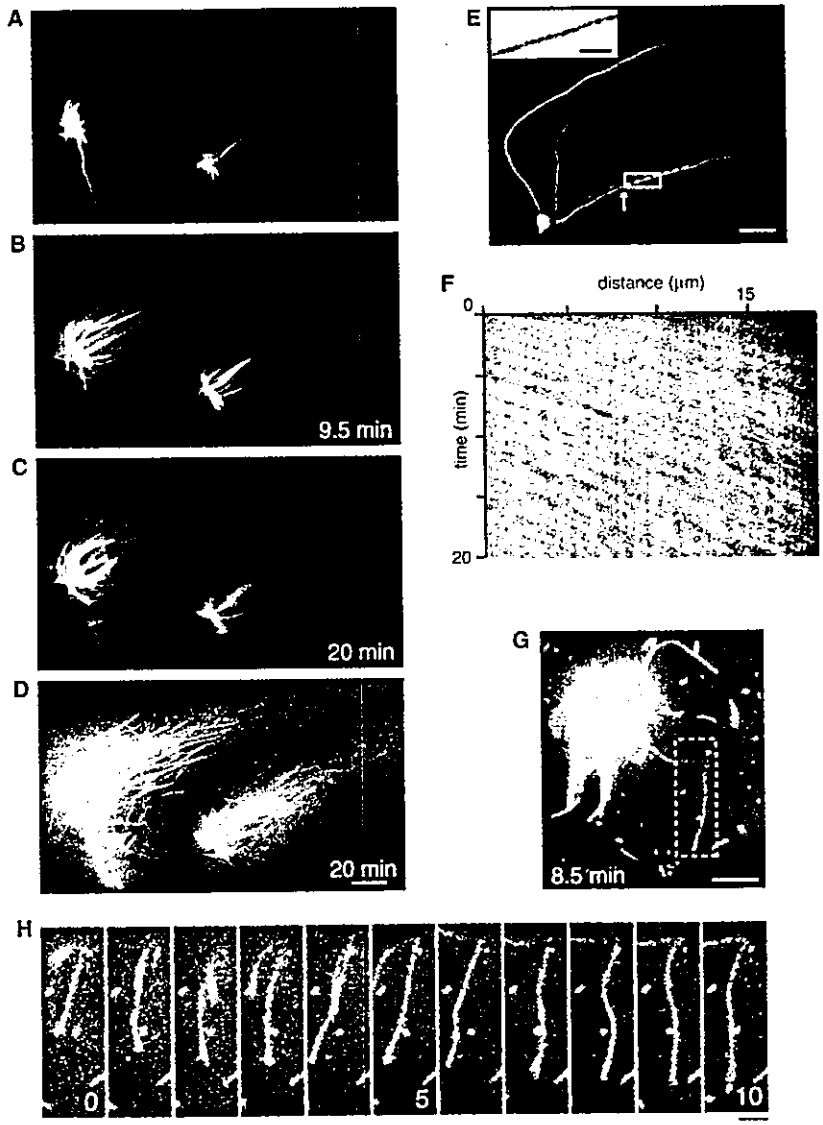

Fig. 4. Actin filament growth emanating from recombinant mDia1ΔN3. GST-mDia1ΔN3 was labeled using a GST-specific goat antibody and an Alexa594antibody directed against goat IgG, and then mixed with 1.9 μM actin and 1.3 μM profilin in buffer [20 mM imidazole (pH 7.0), 2 mM Tris HCl, 0.2 mM ATP, 2.1 mM $MgCl_2$, 2 mM EGTA, 100 mM KCl, 10.5 mM DTT, 0.1 mg/ml glucose oxidase, 3 mg/ml glucose, 20 μg/ml catalase, 0.5% methylcellulose, 83 nM Oregon Green-phalloidin]. (A to D) Time-lapse images of actin filament outgrowth (A to C). Merged image of F-actin (green) and GST-mDia1ΔN3 (red) (D). Time relative to (A) is shown. (E and F) Speckle labeling of the filaments revealing fast filament elongation at GST-mDia1ΔN3. Merged image of GST-mDia1ΔN3 (red) and F-actin (green). A part of the phalloidin label image (square) is enlarged [(E), inset, scale bar, 2 μm]. Actin filaments moved initially at ~0.040 μm/s. Conditions were the same except for 4.2 nM Oregon Green-phalloidin. Scale bar, 10 μm. Kymograph (F) shows cross-sectional view of the intensity values along the dashed line. Distance is from arrow in (E). (G and H) Persistent growth of a single actin filament anchored to mDia1ΔN3. (G) F-actin (green) and GST-mDia1ΔN3 (red). Scale bar, 5 μm. (H) Time-lapse images of phalloidin-staining (dashed square) are paneled. Time is in minutes. Scale bar, 2 μm.

References and Notes

1. M. Evangelista, S. Zigmond, C. Boone, *J. Cell Sci.* **116**, 2603 (2003).
2. B. J. Wallar, A. S. Alberts, *Trends Cell Biol.* **13**, 435 (2003).
3. D. H. Castrillon, S. A. Wasserman, *Development* **120**, 3367 (1994).
4. F. Chang, D. Drubin, P. Nurse, *J. Cell Biol.* **137**, 169 (1997).
5. M. Evangelista, D. Pruyne, D. C. Amberg, C. Boone, A. Bretscher, *Nature Cell Biol.* **4**, 32 (2002).
6. I. Sagot, S. K. Klee, D. Pellman, *Nature Cell Biol.* **4**, 42 (2002).
7. H. Imamura *et al.*, *EMBO J.* **16**, 2745 (1997).
8. N. Watanabe, T. Kato, A. Fujita, T. Ishizaki, S. Narumiya, *Nature Cell Biol.* **1**, 136 (1999).
9. I. Sagot, A. A. Rodal, J. Moseley, B. L. Goode, D. Pellman, *Nature Cell Biol.* **4**, 626 (2002).
10. D. Pruyne *et al.*, *Science* **297**, 612 (2002).
11. M. Pring, M. Evangelista, C. Boone, C. Yang, S. H. Zigmond, *Biochemistry* **42**, 486 (2003).
12. D. R. Kovar, J. R. Kuhn, A. L. Tichy, T. D. Pollard, *J. Cell Biol.* **161**, 875 (2003).
13. F. Li, H. N. Higgs, *Curr. Biol.* **13**, 1335 (2003).
14. S. H. Zigmond *et al.*, *Curr. Biol.* **13**, 1820 (2003).
15. N. Watanabe, T. J. Mitchison, *Science* **295**, 1083 (2002).
16. Materials and Methods are available as supporting material on *Science* Online.
17. J. W. Copeland, R. Treisman, *Mol. Biol. Cell* **13**, 4088 (2002).
18. A. S. Alberts, *J. Biol. Chem.* **276**, 2824 (2001).
19. A. J. Ridley, A. Hall, *Cell* **70**, 389 (1992).
20. M. Coue, S. L. Brenner, I. Spector, E. D. Korn, *FEBS Lett.* **213**, 316 (1987).
21. M. R. Bubb, I. Spector, B. B. Beyer, K. M. Fosen, *J. Biol. Chem.* **275**, 5163 (2000).
22. P. Sampath, T. D. Pollard, *Biochemistry* **30**, 1973 (1991).
23. T. D. Pollard, L. Blanchoin, R. D. Mullins, *Annu. Rev. Biophys. Biomol. Struct.* **29**, 545 (2000).
24. M. J. DiNubile, L. Cassimeris, M. Joyce, S. H. Zigmond, *Mol. Biol. Cell* **6**, 1659 (1995).
25. D. A. Schafer, P. B. Jennings, J. A. Cooper, *J. Cell Biol.* **135**, 169 (1996).
26. M. R. Bubb, E. G. Yarmola, B. G. Gibson, F. S. Southwick, *J. Biol. Chem.* **278**, 24629 (2003).
27. F. S. Southwick, C. L. Young, *J. Cell Biol.* **110**, 1965 (1990).
28. H. C. Yang, L. A. Pon, *Proc. Natl. Acad. Sci. U. S. A.* **99**, 751 (2002).
29. T. Adam, M. Giry, P. Boquet, P. Sansonetti, *EMBO J.* **15**, 3315 (1996).
30. J. A. Theriot, *Traffic* **1**, 19 (2000).

31. We thank K. Nonomura for technical assistance. Supported in part by grants-in-aid for Scientific Research from Ministry of Education, Culture, Sports, Science and Technology of Japan and by grants from PRESTO-JST and Takeda Science Foundation.

Supporting Online Material

www.sciencemag.org/cgi/content/full/303/5666/2007/DC1
Materials and Methods
References
Movies S1 to S12

21 November 2003; accepted 26 January 2004

Volume 14, Issue 1 , 9 April 2004, Pages 29-41

doi:10.1016/S1097-2765(04)00153-4 Cite or Link Using DOI

Article

The Small GTP-Binding Protein RhoA Regulates c-Jun by a ROCK-JNK Signaling Axis

Maria Julia Marinissen [1], Mario Chiariello [1,3], Tamara Tanos [2], Ora Bernard [4], Shuh Narumiya [5] and J. Silvio Gutkind [1]

[1] Oral and Pharyngeal Cancer Branch, National Institute of Dental and Craniofacial Research, National Institutes of Health, Bethesda, MD 20892, USA
[2] Facultad de Ciencias Exactas, Universidad de Buenos Aires, Buenos Aires, Argentina
[3] Istituto di Endocrinologia ed Oncologia Sperimentale, CNR, Via Pansini 5, 80131, Napoli, Italy
[4] The Walter and Eliza Hall Institute of Medical Research, 1G Royal Parade Parkville, Victoria 3050, Australia
[5] Department of Pharmacology, Kyoto University Faculty of Medicine, Sakyo-ku, Kyoto 606-8501, Japan

Received 6 November 2003; Revised 23 February 2004; accepted 25 February 2004
Published: April 8, 2004 Available online 7 April 2004.

Abstract

RhoA regulates the actin cytoskeleton and the expression of genes associated with cell proliferation. This includes c-*fos* and c-*jun*, which are members of the AP1 family of transcription factors that play a key role in normal and aberrant cell growth. Whereas RhoA stimulates the c-*fos* SRE by a recently elucidated mechanism that is dependent on actin treadmilling, how RhoA regulates c-*jun* is still poorly understood.

We found that RhoA stimulates c-*jun* expression through ROCK, but independently from the ability of ROCK to promote actin polymerization. Instead, we found that ROCK activates JNK, which then phosphorylates c-Jun and ATF2 when bound to the c-*jun* promoter. Thus, ROCK represents a point of signal divergence downstream from RhoA, as it promotes actin reorganization and the consequent expression from the c-*fos* SRE, while a parallel pathway connects ROCK to JNK, thereby stimulating c-*jun* expression. Ultimately, these pathways converge in the nucleus to regulate AP1 activity.

Corresponding author. Correspondence: J. Silvio Gutkind, 301 496 6259 (phone), 301 402 0823 (fax)

Cdc42 and mDia3 regulate microtubule attachment to kinetochores

Shingo Yasuda[1,2], Fabian Oceguera-Yanez[1], Takayuki Kato[1]*, Muneo Okamoto[1], Shigenobu Yonemura[3], Yasuhiko Terada[4], Toshimasa Ishizaki[1] & Shuh Narumiya[1]

[1]*Department of Pharmacology and* [2]*Horizontal Medical Research Organization, Kyoto University Faculty of Medicine, Kyoto 606-8501, Japan*
[3]*Laboratory for Cellular Morphogenesis, RIKEN Center for Developmental Biology, Kobe 650-0047, Japan*
[4]*Department of Genetics, Cell Biology and Development, University of Minnesota, Minnesota 55455, USA*

* Present address: Department of Physiology, Osaka City University Medical School, Osaka 545-8585, Japan

During mitosis, the mitotic spindle, a bipolar structure composed of microtubules (MTs) and associated motor proteins[1,2], segregates sister chromatids to daughter cells. Initially some MTs emanating from one centrosome attach to the kinetochore at the centromere of one of the duplicated chromosomes. This attachment allows rapid poleward movement of the bound chromosome. Subsequent attachment of the sister kinetochore to MTs

growing from the other centrosome results in the bi-orientation of the chromosome, in which interactions between kinetochores and the plus ends of MTs are formed and stabilized[2]. These processes ensure alignment of chromosomes during metaphase and their correct segregation during anaphase. Although many proteins constituting the kinetochore have been identified and extensively studied, the signalling responsible for MT capture and stabilization is unclear[1,2]. Small GTPases of the Rho family regulate cell morphogenesis by organizing the actin cytoskeleton and regulating MT alignment and stabilization[3]. We now show that one member of this family, Cdc42, and its effector, mDia3, regulate MT attachment to kinetochores.

Although Rho participates in cytokinesis[3,4], whether Rho GTPases contribute to nuclear division remains unclear. To examine the possibility that Rho GTPases do take part, we synchronized HeLa cells in prometaphase of mitosis using nocodazole, and incubated the nocodazole-arrested cells with *Clostridium difficile* toxin B, which inactivates all Rho GTPases including Rho, Rac and Cdc42[5]. Cells were able to progress through mitosis when nocodazole was removed. Staining for DNA, MTs and a kinetochore protein, CENP-A[2], revealed that toxin B treatment markedly prevented chromosome alignment at metaphase (Fig. 1a). Even 90 min after nocodazole removal, when control cells had progressed to anaphase and telophase, the chromosomes of many toxin-treated cells were widely scattered, with several chromosomes clustering near the poles despite most cells retaining a bipolar spindle. Scattered chromosomes were often mono-oriented (Fig. 1a, insets 1 and 2) or orientated with an apparent lack of MT attachment (Fig. 1a, inset 3). Staining for Mad-2, a mitotic spindle-checkpoint protein[2], verified the loss of MT attachment to these chromosomes (Fig. 1b), which was further confirmed by electron microscopy (Supplementary Information). The cells with misaligned chromosomes decreased gradually from 90% of the population at 60 min to 50% at 180 min (Fig. 1c). Video microscopy (Supplementary Movies 1 and 2) revealed that the chromosomes of toxin-B-treated cells moved without congression during the entire observation period of 250 min, and that some exited to interphase without a distinct anaphase to produce abberant tetraploid nuclei. This progression to interphase was accompanied by cyclin B degradation (Supplementary Information), suggesting that the toxin B treatment affected the spindle-checkpoint mechanism.

The above findings implicated a Rho family GTPase in MT

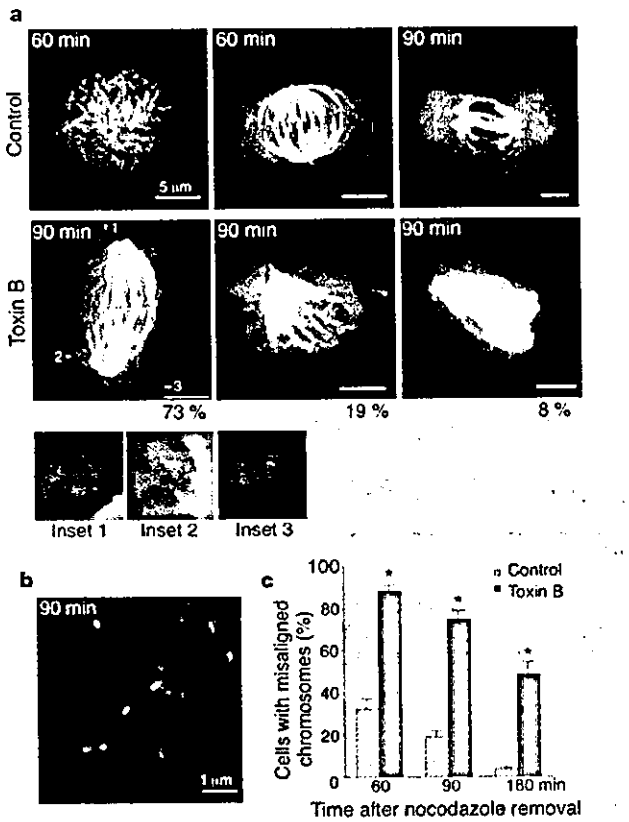

Figure 1 Effects of toxin B on mitosis. **a**, Chromosome misalignment in toxin-B-treated cells. Control or toxin-B-treated HeLa cells were fixed at the times indicated after nocodazole removal and stained. β-tubulin, green; CENP-A, red; DNA, blue. The numbers below the lower panels (**a**) indicate the percentage of cells exhibiting (from left to right) the bipolar, monopolar and multipolar spindle, respectively ($n = 300$). The insets show the parts of the image indicated by the numbered arrows in the above figure. **b**, MAD2 staining of toxin-B-treated cells 90 min after removal of nocodazole. CENP-A, red; MAD2, green; DNA, blue. **c**, Percentage of cells with misaligned chromosomes. Data are means ± s.e.m. from 100 cells at each time point ($n = 5$). *$P < 0.05$ versus control experiment.

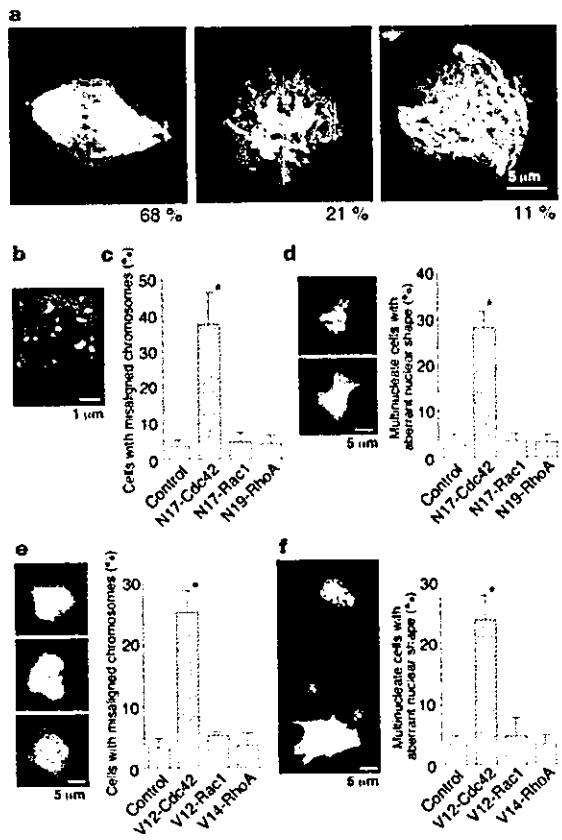

Figure 2 Effects of Rho GTPase mutants on mitosis. **a**, **b**, Chromosome misalignment (**a**) and MAD2 staining (**b**) of N17-Cdc42 expressing cells. Staining is the same as in Fig. 1. The numbers shown in **a** indicate the percentage of cells with abnormal mitosis exhibiting (from left to right) the bipolar, monopolar and multipolar spindle, respectively ($n = 98$). **c**, **d**, Percentages of cells with chromosome misalignment (**c**) or aberrant multiple nuclei (**d**) among cells expressing green fluorescent protein (GFP) alone (control) or the GFP fusion of N17-Cdc42, N17-Rac1 or N19-RhoA in mitosis or interphase. The left panel in **d** shows an N17-Cdc42 expressing multinucleate cell (β-tubulin, red; DNA, blue). **e**, **f**, Chromosome misalignment (**e**) and production of multinucleate cells (**f**) by expression of V12-Cdc42 in NIH 3T3 cells. The percentages of cells with misaligned chromosomes or multiple nuclei among cells expressing GFP alone (control) or GFP fusion of V12-Cdc42, V12-Rac1 or V14-RhoA were analysed at mitosis (**e**) or interphase (**f**). Left panels show images of cells expressing V12-Cdc42 and stained for β-tubulin and DNA as in **d**. Data in **c**–**f** are means ± s.e.m. of 100 cells for each condition ($n \geq 3$, each). *$P < 0.05$ versus control cells.

attachment and chromosome alignment during mitosis, therefore we examined the effects of dominant-negative mutants of Rho GTPases on mitosis. HeLa cells were synchronized at the beginning of S phase using a double-thymidine block and transfected with complementary DNAs for the mutant proteins during the middle of the second block. Most cells entered mitosis 12 h after thymidine removal. Cells expressing the dominant-negative N17-Cdc42 mutant exhibited chromosome misalignment similar to that in toxin-B-treated cells (Fig. 2a). Again, Mad2 localized to kinetochores of the misaligned chromosomes, indicating that MTs failed to attach to the kinetochores (Fig. 2b). These abnormalities were detected in >35% of cells expressing N17-Cdc42 (Fig. 2c). By contrast, the proportion of cells with these phenotypes was less than 5% in control cells transfected with the empty vector and those expressing the dominant-negative N19-RhoA or N17-Rac1 mutants. Sixteen hours after thymidine removal, multinucleate cells with macro- and micronuclei and nuclear bridges were frequently observed among interphase cells expressing N17-Cdc42 (Fig. 2d), indicating that the chromosome misalignment in these cells led to missegregation of chromosomes. By contrast, and consistent with previous reports[4,6], expression of N19-RhoA caused cytokinesis failure, producing cells with two nuclei of equal size (data not shown). No phenotype was apparent in cells expressing N17-Rac1 (data not shown). Chromosome misalignment and generation of multinucleate cells were also induced by expression of a dominant-active mutant of Cdc42 (V12-Cdc42) (Fig. 2e, f), but not of Rac1 or RhoA. These results suggest that Cdc42 is essential for MT-mediated chromosome alignment in mammalian cells, and that either inhibition or enhancement of its activity causes chromosome misalignment, prometaphase delay and chromosome missegregation.

We next attempted to identify the downstream target of Cdc42 in this action. A candidate was the Rho effector mDia, a mammalian homologue of *Drosophila* diaphanous and a member of the formin-homology (FH) family of proteins, which are conserved from yeast to mammals[7]. This family of proteins induces actin polymerization and promotes the alignment and stabilization of MTs[8–10]. There are three mDia isoforms (mDia1[8], mDia2[11] and mDia3/hDia2[12]), all of which contain a Rho-binding domain (RBD) and the highly conserved FH1, FH2 and FH3 regions (Fig. 3a).

Using a yeast two-hybrid assay, we found that the FH2 region of mDia isoforms binds to CENP-A[2,15] and a different region of mDia binds to another centromere–kinetochore protein, heterochromatin protein (HP) 1[16] (Fig. 3a and Supplementary Information). We also found that among the three isoforms only mDia3 can bind to Cdc42, as well as to RhoA and Rac1, in a GTP-dependent manner (Fig. 3b and Supplementary Information). These results suggest that mDia3 is a target of Cdc42 at the kinetochore. Consistently, we found mDia3 in the prekinetochore complex precipitated with an anti-CENP-A antibody[17] from nuclear digests but not in the control pellets (Fig. 3c).

An immunofluorescence study using a specific anti-mDia3 antibody (Supplementary Information) detected mDia3 signals as punctae in the nucleus of interphase cells that colocalized with

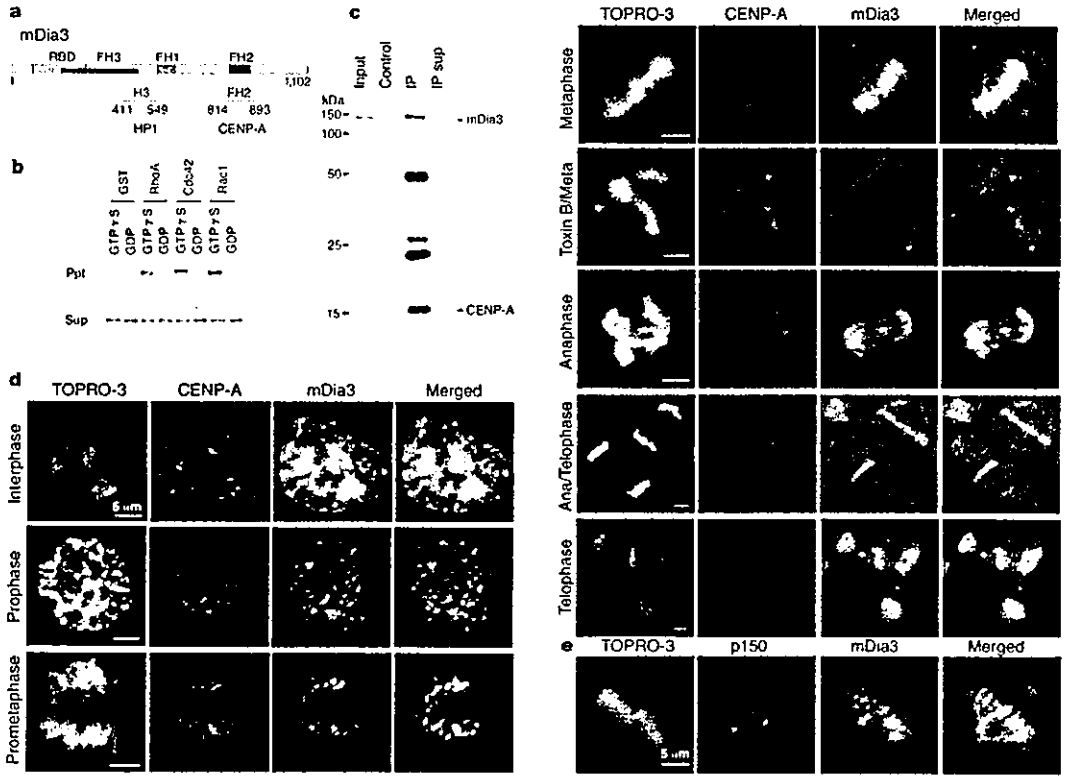

Figure 3 Interaction of mDia3 and CENP-A. **a**, Domain structure of mDia3. The regions interacting with HP-1 and CENP-A are indicated. **b**, GTP-dependent binding of mDia3 to Rho GTPases. An *in vitro* precipitation assay between the RBD of mDia3 and Rho GTPases bound to GDP or GTPγS is shown. **c**, Co-precipitation of mDia3 and CENP-A in the prekinetochore complex. Nuclear digests were precipitated by control beads or anti-CENP-A antibody (IP) and probed with antibodies to mDia3 (above) or CENP-A (below). **d**, Localization of mDia3 in mitosis. HeLa cells were fixed at the indicated phases and stained for mDia3 (green), CENP-A (red) and DNA (TOPRO-3). Toxin B/meta, a toxin B-treated mitotic cell. **e**, Co-staining for mDia3 (green) and p150^{Glued} (red) in mitotic cells.

HP-1 signals (Supplementary Information) and partially overlapped with those of CENP-A (Fig. 3d). More of the mDia3 signals overlapped with CENP-A during prophase nuclei, and they were present together at kinetochores of condensed chromosomes in prometaphase cells (Fig. 3d). During metaphase, mDia3 signals were still associated with CENP-A (Fig. 3d) and were juxtaposed with those of $p150^{Glued}$, a component of the dynactin–dynein complex that anchors MTs to the kinetochore[2] (Fig. 3e). Toxin B treatment abolished mDia3 signals at the kinetochore without affecting CENP-A localization (Fig. 3d), indicating that endogenous Cdc42 localizes mDia3 at the kinetochore in metaphase chromosomes. By contrast, mDia3 localization was not affected by active Cdc42 expression (data not shown), suggesting that dominant-active Cdc42 causes chromosome misalignment not by displacement of mDia3 from the kinetochore but instead by activating mDia3 homogenously in the cell, thereby decreasing the significance of endogenous Cdc42. During anaphase, some mDia3 signals moved poleward with CENP-A, but some migrated to both polar and midzone spindle MTs. The signals in the midzone became condensed during late anaphase and accumulated in the midbody in telophase. Thus, a subpopulation of mDia3 behaved like a chromosomal passenger protein[18]. By contrast, mDia1 was localized predominantly in the cytoplasm of interphase cells, and was enriched in the polar spindle MTs and the cell cortex of mitotic cells, as previously described[8,14] (Supplementary Information).

We next investigated the role of mDia3 during mitosis. We transfected HeLa cells with a small interfering RNA (siRNA) duplex targeted to a region of mDia3 messenger RNA. As controls, we used siRNA with a scrambled sequence or targeted to mDia1 mRNA[19]. Treatment with siRNA for mDia1 and mDia3 resulted in a marked decrease in the respective proteins as detected by immunoblotting (Fig. 4a) and confirmed by immunofluorescence (Supplementary Information). Examination 36 h after transfection revealed that the mitotic index of the mDia3 RNAi cells increased significantly, to 25%, whereas control cells had a mitotic index of 8 to 9% (Fig. 4b). In this mitotic population of mDia3 RNAi cells, a marked increase in the percentage of cells in prometaphase and a concomitant decrease in those in metaphase, anaphase or telophase was found (Fig. 4c).

Video microscopy of these prometaphase-arrested cells found that most of them had established bipolar spindles, but many chromosomes remained scattered at the poles (Fig. 4d; Supplementary Movies 3–5). This is the same phenotype found in cells treated with toxin B or expressing N17-Cdc42. To identify the mechanism underlying this abnormality, we stained for EB1, a plus-end MT-binding protein that is important for spindle MT stabilization[2]. Consistent with previous reports[20,21], some EB1 signals in control cells colocalized with those of CENP-A on metaphase chromosomes. However, they barely overlapped with CENP-A signals in cells treated with either siRNA for mDia3 or toxin B (Fig. 4e). In addition to these findings, we also noted that expression of a dominant-active form of mDia3 in mitotic NIH 3T3 cells induced chromosomal misalignment and resulted in production of multinucleate cells (Supplementary Information).

We have shown involvement of Cdc42 and its effector mDia3 in MT-mediated chromosome alignment. This role for Cdc42, although unexpected, is consistent with several observations. For example, although not explicitly stated, expression of dominant-negative forms of ECT2 or MgcRacGAP, a putative activator and downregulator, respectively, of Rho GTPases in mitosis, induced the formation of tetraploid nuclei with abnormal shape[22,23]. Homozygous disruption of the mouse *MgcRacGAP* gene resulted in death of day 3.5 to 4 embryos owing to the failure of chromosomal segregation[24]. Using a pull-down assay, we found that Cdc42 was activated at metaphase, and this activation was regulated by Ect2 and MgcRacGAP (unpublished observation). Roles for Cdc42, mDia and homologues, often in conjunction with EB1 and its binding partner, adenomatous polyposis coli protein (APC), in the regulation of MT alignment have been reported previously, in yeast[25] and mammalian cells[9,10,26]. Notably, mDia1 induces MT alignment and stabilization at the cell cortex through EB1 in mammalian cells[9,10]. Therefore, it appears that similar mecha-

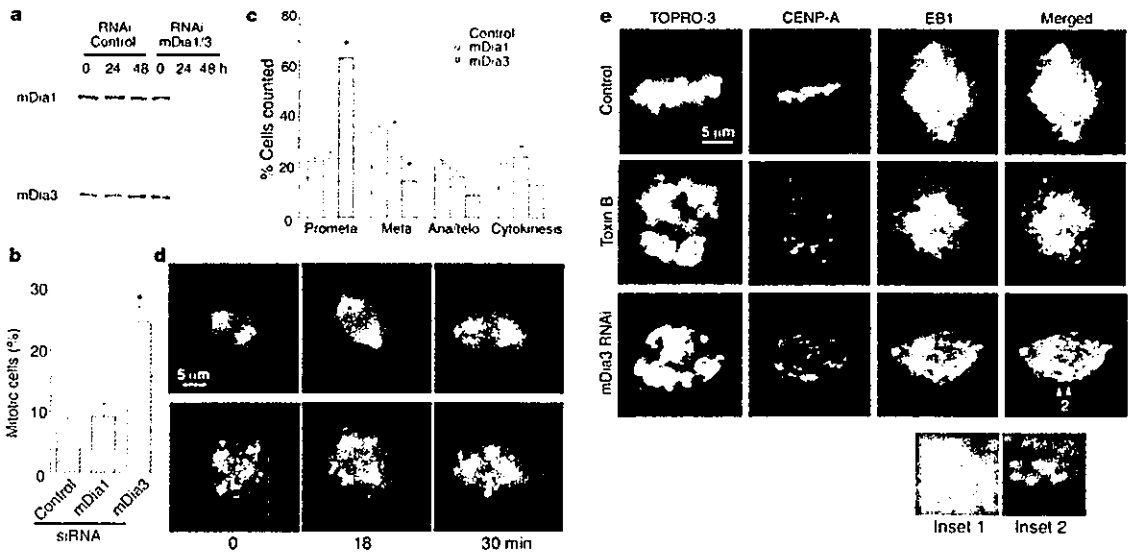

Figure 4 Effects of depletion of mDia3 on mitosis. **a**, Depletion of mDia1 and mDia3 by RNA interference. Immunoblots of cells subjected to RNAi with antibodies to mDia1 and mDia3 are shown. **b**, **c**, Increase of the mitotic index and prometaphase arrest in mDia3 RNAi cells. The mitotic index of 300 cells subjected to indicated RNAi in three independent experiments (**b**), and the proportion of the cells in each phase of mitosis (**c**) are shown as means ± s.e.m. $^*P < 0.05$ versus the control cells. **d**, Video microscopy. Cells with GFP–EB-1-labelled MTs (green) and with dsRed2-histone H2B-k-labelled chromosomes (red) were subjected to RNAi for mDia3, and progression through mitosis was monitored by video-microscopy. Images for GFP–EB1 alone are shown above. (Movies available online as Supplementary Movies 3–5.) **e**, Loss of EB1 signals at kinetochores in cells treated with toxin B or subjected to RNAi for mDia3. The insets show parts of the images indicated by the numbered arrows in the figures.

nisms operate during MT attachment to the cell cortex and kinetochores. APC and EB1 are also important for MT attachment to kinetochores[2,27]. MTs attach first to one of the kinetochore pair of the chromosomes, causing translocation of chromosomes to the corresponding pole. MT attachment then occurs in a bi-oriented manner and is stabilized[2,28]. In cells with impaired Cdc42–mDia3 signalling, many chromosomes accumulate near each pole and are either mono-oriented or without MT attachment. These findings indicate that the Cdc42–mDia3 signalling is not involved in the initial attachment of MTs to kinetochores but plays an important role in subsequent, stable bi-orientated MT attachment for proper chromosome alignment and segregation. Whether such a role for the Cdc42–mDia3 signalling is limited to mammalian cells remains to be seen. □

Methods

Materials

Sources and construction of plasmid DNAs are described in Supplementary Information. The mDia1 siRNA was described previously[19], and the mDia3 siRNA corresponded to nucleotides 172 to 190 of the mRNA relative to the translation initiation codon.

Cell culture and transfection

HeLa cells and NIH 3T3 cells were maintained at 37 °C in Dulbecco's modified Eagle's medium (GIBCO-BRL) supplemented with 10% fetal bovine serum and penicillin–streptomycin. Cells were synchronized in S phase by the double-thymidine block protocol (two cycles of 15 h culture with thymidine and 9 h culture free of thymidine); enrichment of mitotic cells was achieved by nocodazole treatment after release from the thymidine block[29]. When transfection was performed during the second thymidine block, HeLa cells were washed 9 h after the initiation of the second thymidine block, transfected in Opti-MEM with the use of Lipofectamine Plus (GIBCO-BRL) for 2 h, and cultured again in the original culture medium for 4 h in the continued presence of thymidine before thymidine removal. Expression in NIH3T3 cells was carried out by microinjection of plasmid DNA immediately after thymidine removal.

Microscopy

For immunofluorescence, cells were fixed in methanol at −20 °C. For kinetochore staining, cells were permeabilized for 5 min with 0.005% digitonin in a solution containing 110 mM potassium acetate, 20 mM HEPES (pH 7.3), 2 mM magnesium acetate, 0.5 mM EGTA and 2 mM dithiothreitol before fixation. Immunostaining was performed as described previously[9]. Primary antibodies included those against mDia3 (goat, 1:50 dilution; Santa Cruz Biotechnology), mDia1[19] (rabbit; 1:200 dilution), α-tubulin (DM1A, mouse, 1:100 dilution; Sigma), β-tubulin (TUB2.1, mouse, 1:100 dilution; Sigma), MAD2 (rabbit, 1:500 dilution; COVANCE), CENP-A (human CREST serum, 1:1,000 dilution), p150^{Glued} (mouse, 1:200 dilution; Transduction Laboratories) and EB1 (mouse, 1:200 dilution; Transduction Laboratories). Immune complexes were detected with appropriate secondary antibodies labelled with either Alexa488, Alexa594 or Alexa633 (Molecular Probes). DNA was stained with Hoechst 33342 (1 μg ml^{-1}), DAPI or TOPRO-3 (Molecular Probes). Cells were examined with a Zeiss LSM510 confocal imaging system or a DeltaVision microscope system. Electron microscopy was carried out as described previously[30].

Assays for protein interaction and staining

Two-hybrid assays were performed as described previously[19] with the plasmids described above. The L40 yeast strain was cotransfected with pBTM and either pVP16 or pACT2 vectors, and protein interaction was detected by staining with the β-galactosidase substrate X-gal. Coprecipitation ('pull-down') assays were performed using recombinant glutathine-*S*-transferase–Rho GTPases and thioredoxin-tagged RBDs as described previously[19]. For chromatin immunoprecipitation, 5 × 10^7 HeLa cells were harvested and homogenized in 10 mM Tris.HCl containing 10 mM NaCl, 3 mM $MgCl_2$ and 0.5% NP-40. Isolated nuclei were suspended in nuclei-washing buffer and were digested for 1 h at 37 °C with 80 U micrococcal nuclease[17]. The digests were centrifuged at 10,000*g* for 10 min, and the supernatant was subjected to precipitation with mouse monoclonal anti-CENP-A antibody[17]. The immunoprecipitates were recovered and probed with antibodies to CENP-A and mDia3. Western blot analysis was performed using an anti-cyclin B1 antibody (clone CB169, Upstate biotechonology) or antibodies to mDia1 and mDia3 as described previously[9].

Received 11 December 2003; accepted 1 March 2004; doi:10.1038/nature02452.

1. Scholey, J. M., Brust-Mascher, I. & Mogilner, A. Cell division. *Nature* **422**, 746–752 (2003).
2. Cleveland, D. W., Mao, Y. & Sullivan, K. F. Centromeres and kinetochores: from epigenetics to mitotic checkpoint signaling. *Cell* **112**, 407–421 (2003).
3. Etienne-Manneville, S. & Hall, A. Rho GTPases in cell biology. *Nature* **420**, 629–635 (2002).
4. Mabuchi, I. *et al.* A rho-like protein is involved in the organisation of the contractile ring in dividing sand dollar eggs. *Zygotes* **1**, 325–331 (1993).
5. Just, I. *et al.* Glucosylation of Rho proteins by *Clostridium difficile* toxin B. *Nature* **375**, 500–503 (1995).
6. Eda, M. *et al.* Rho-dependent transfer of Citron-kinase to the cleavage furrow of dividing cells. *J. Cell Sci.* **114**, 3273–3284 (2001).
7. Wasserman, S. FH proteins as cytoskeletal organizers. *Trends Cell Biol.* **8**, 111–115 (1998).
8. Watanabe, N. *et al.* p140mDia, a mammalian homolog of *Drosophila* diaphanous, is a target protein for Rho small GTPase and is a ligand for profilin. *EMBO J.* **16**, 3044–3056 (1997).
9. Ishizaki, T., Morishima, Y., Furuyashiki, T., Kato, T. & Narumiya, S. Coordination of microtubules and actin cytoskeleton by a Rho effector, mDia1. *Nature Cell Biol.* **3**, 8–14 (2001).
10. Gundersen, G. G. Evolutionary conservation of microtubule-capture mechanisms. *Nature Rev. Mol. Cell. Biol.* **3**, 296–304 (2002).
11. Alberts, A. S., Bouquin, N., Johnston, L. H. & Treisman, R. Analysis of RhoA-binding proteins reveals an interaction domain conserved in heterotrimeric G protein β subunits and the yeast response regulator protein Skn7. *J. Biol. Chem.* **273**, 8616–8622 (1998).
12. Bione, S. *et al.* A human homologue of the *Drosophila melanogaster* diaphanous gene is disrupted in a patient with premature ovarian failure: evidence for conserved function in oogenesis and implications for human sterility. *Am. J. Hum. Genet.* **62**, 533–541 (1998).
13. Watanabe, N. *et al.* Cooperation between mDia1 and ROCK in Rho-induced actin reorganization. *Nature Cell Biol.* **1**, 136–143 (1999).
14. Kato, T. *et al.* Localization of a mammalian homolog of Diaphanous, mDia1, to the mitotic spindle in HeLa cells. *J. Cell Sci.* **114**, 775–784 (2001).
15. Goshima, G., Kiyomitsu, T., Yoda, K. & Yanagida, M. Human centromere chromatin protein hMis12, essential for equal segregation, is independent of CENP-A loading pathway. *J. Cell Biol.* **160**, 25–39 (2003).
16. Kellum, R. HP1 complexes and heterochromatin assembly. *Curr. Top. Microbiol. Immunol.* **274**, 53–77 (2003).
17. Ando, S. *et al.* CENP-A, -B, and -C chromatin complex that contains the I-type α-satellite array constitutes the prekinetochore in HeLa cells. *Mol. Cell. Biol.* **22**, 2229–2241 (2002).
18. Adams, R. R., Carmena, M. & Earnshaw, W. C. Chromosomal passengers and the (aurora) ABCs of mitosis. *Trends Cell. Biol.* **11**, 49–54 (2001).
19. Arakawa, Y. *et al.* Control of axon elongation via an SDF-1α/Rho/mDia pathway in cultured cerebellar granule neurons. *J. Cell Biol.* **161**, 381–391 (2003).
20. Tirnauer, J. S., Canman, J. C., Salmon, E. D. & Mitchison, T. J. EB1 targets to kinetochores with attached, polymerizing microtubules. *Mol. Biol. Cell* **13**, 4308–4316 (2002).
21. Anand, S., Penrhyn-Lowe, S. & Venkitaraman, A. R. AURORA-A amplification overrides the mitotic spindle assembly checkpoint, inducing resistance to Taxol. *Cancer Cell* **3**, 51–62 (2003).
22. Tatsumoto, T., Xie, X., Blumenthal, R., Okamoto, I. & Miki, T. Human ECT2 is an exchange factor for Rho GTPases, phosphorylated in G2/M phases, and involved in cytokinesis. *J. Cell Biol.* **147**, 921–928 (1999).
23. Hirose, K. *et al.* MgcRacGAP is involved in cytokinesis through associating with mitotic spindle and midbody. *J. Biol. Chem.* **276**, 5821–5828 (2001).
24. Van de Putte, T. *et al.* Mice with a homozygous gene trap vector insertion in *mgcRac GAP* die during pre-implantation development. *Mech. Dev.* **102**, 33–44 (2001).
25. Rodriguez, O. C. *et al.* Conserved microtubule-actin interactions in cell movement and morphogenesis. *Nature Cell Biol.* **5**, 599–609 (2003).
26. Etienne-Manneville, S. & Hall, A. Cdc42 regulates GSK-3β and adenomatous polyposis coli to control cell polarity. *Nature* **421**, 753–756 (2003).
27. Pellman, D. Cancer. A CINtillating new job for the APC tumor suppressor. *Science* **291**, 2555–2556 (2001).
28. Yao, X. *et al.* CENP-E forms a link between attachment of spindle microtubules to kinetochores and the mitotic checkpoint. *Nature Cell Biol.* **2**, 484–491 (2000).
29. Andreassen, P. R., Palmer, D. K., Wener, M. H. & Marholis, R. L. Telophase disc: a new mammalian mitotic organelle that bisects telophase cells with a possible function in cytokinesis. *J. Cell Sci.* **99**, 523–534 (1991).
30. Maiato, H. *et al.* Human CLASP1 is an outer kinetochore component that regulates spindle microtubule dynamics. *Cell* **113**, 891–904 (2003).

Supplementary Information accompanies the paper on **www.nature.com/nature.**

Acknowledgements We thank K. Aktories for *Clostridium difficile* toxin B, Y. Kiyosue for pQBI25-Xβ-tubulin, N. Mimori for CREST serum, S. Tsukita for the use of Delta-Vision system, T. Kiyomitsu, T. Tsuji, Y. Arakawa, J. Monypenny and N. Watanabe for advice, and M. Yanagida for discussion. This work was supported in part by Grants-in-aid for Scientific Research from the Ministry of Education, Culture, Sports, Science and Technology of Japan and from the Ministry of Health, Labour and Welfare of Japan.

Competing interests statement The authors declare that they have no competing financial interests.

Correspondence and requests for materials should be addressed to S.N. (snaru@mfour.med.kyoto-u.ac.jp).

Cell Cycle. 2004 Jul;3(7):855-7. Epub 2004 Jul 25.

A new look at Rho GTPases in cell cycle: role in kinetochore-microtubule attachment.

Narumiya S, Oceguera-Yanez F, Yasuda S.

Department of Pharmacology, Kyoto University Faculty of Medicine, Kyoto, Japan. snaru@mfour.med.kyoto-u.ac.jp

Rho GTPases including Rho, Rac and Cdc42 are involved in cell morphogenesis by inducing specific types of actin cytoskeleton and alignment and stabilization of microtubules. Previous studies suggest that they also regulate cell cycle progression; Rho, Rac and Cdc42 regulate the G(1)-S progression and Rho controls cytokinesis. However, a role of Rho GTPases in nuclear division has not been definitely shown.We have recently found that Cdc42 and its downstream effector mDia3 are involved in bi-orientation and stabilization of spindle microtubules attachment to kinetochores and regulate chromosome alignment and segregation. Here, we discuss how this is coordinated with other events in mitosis, particularly, with the action of Rho in cytokinesis and how attachment of microtubules to kinetochores is achieved and stabilized. We also discuss redundancy of dc42 and Cdc42-related GTPase(s) and potential mechanisms of chromosome instability in cancer.

Available online at www.sciencedirect.com
SCIENCE DIRECT
Experimental Cell Research 298 (2004) 207–217
Experimental Cell Research
www.elsevier.com/locate/yexcr

$G\alpha_{q/11}$ signaling induces apoptosis through two pathways involving reduction of Akt phosphorylation and activation of RhoA in HeLa cells

Hiroshi Ueda,[a] Rika Morishita,[a] Shuh Narumiya,[b] Kanefusa Kato,[a] and Tomiko Asano[a,*]

[a] *Department of Molecular Neurobiology, Institute for Developmental Research, Aichi Human Service Center, Kamiya-cho, Kasugai, Aichi 480-0392, Japan*
[b] *Department of Pharmacology, Kyoto University Faculty of Medicine, Kyoto 606-8315, Japan*

Received 19 May 2003, revised version received 7 April 2004
Available online 18 May 2004

Abstract

We have previously reported that expression of the constitutively active mutant of $G\alpha_{11}$ or stimulation of m1 muscarinic acetylcholine receptor induced proteolytic activation of Rho-associated kinase (ROCK-I) by caspase and apoptosis in HeLa cells. In this study, we investigate the molecular mechanisms of $G\alpha_{q/11}$-induced apoptosis in m1 muscarinic acetylcholine receptor-expressing HeLa cells. Overexpression of Bcl-2 inhibited carbachol-induced ROCK-I cleavage, indicating a mitochondrial apoptotic pathway. Overexpression of the constitutively active mutant of Akt that delivers an anti-apoptotic survival signal had a similar influence. Insulin, a major survival factor in many cells, strongly increased phosphorylation of Akt, which was completely blocked by carbachol. This latter effect was partially inhibited by treatment with the tyrosine phosphatase inhibitors, orthovanadate and pervanadate. In parallel with these observations, carbachol attenuated insulin-stimulated tyrosine phosphorylation of insulin receptor substrate-1, an effect eliminated by orthovanadate. On the other hand, carbachol induced rapid stimulation of endogenous RhoA, and expression of a constitutively active mutant of RhoA increased ROCK-I cleavage. Orthovanadate and the dominant negative mutant of RhoA partially, and their combination completely, inhibited carbachol-induced ROCK-I cleavage and apoptosis. These results demonstrate that $G_{q/11}$ signaling induces apoptosis by reducing insulin-stimulated Akt phosphorylation through tyrosine dephosphorylation and activating RhoA in HeLa cells.

Keywords: Apoptosis; $G\alpha_{q/11}$; Carbachol; Akt; Rho; Protein tyrosine phosphatase; Insulin; IRS-1

Introduction

Heterotrimeric GTP-binding proteins (G proteins) play key roles as modulators in intracellular signal transduction from cell surface G protein-coupled receptors [1,2]. The α subunits of G proteins comprising four major families, G_s, G_i, G_q, and G_{12}, have a guanine nucleotide-binding site and intrinsic GTPase activity. When the associated receptors are activated by stimuli, exchange of a guanine nucleotide from GDP to GTP occurs, and G protein heterotrimers dissociate into Gα and Gβγ, both of which then interact with and regulate effectors, such as adenylyl cyclase and phospholipase Cβ as well as K^+ and Ca^{2+} channels [1,2].

Recent studies have shown that $G_{q/11}$ signals regulate apoptosis in several cell types [3–5]. In cultured neonatal myocytes, many hormones or growth factors that couple to $G_{q/11}$, or overexpression of the wild-type $G\alpha_q$ stimulates cardiomyocyte hypertrophy [3,4]. Hypertrophy or apoptosis of cardiomyocytes was observed in mice overexpressing the wild-type or constitutively active form of $G\alpha_q$ or α_1-adrenergic receptors that are coupled to G_q [3,4,6,7]. In addition, expression of the constitutively active form of G_q was found to cause apoptosis in COS-7 and CHO cells [5]. We have previously shown that overexpression of a constitutively active mutant $G\alpha_{11}$ or stimulation of the m1 muscarinic acetylcholine (m1) receptor by carbachol induces apoptosis in HeLa cells [8]. During apoptosis, activated caspase 3 cleaves and stimulates a Rho kinase, ROCK-I, which contributes to morphological changes such as cell contraction and membrane blebbing [8–10]. There have been several studies on the molecular mechanisms of $G_{q/11}$-induced apoptosis. G_q-induced apoptosis is dependent on protein kinase C in COS-7 and CHO cells [5], and angiotensin II-induced myocyte apoptosis is dependent on the

* Corresponding author. Fax: +81-568-88-0829.
E-mail addresses: toasano@inst-hsc.jp (T. Asano).

0014-4827/$ - see front matter © 2004 Elsevier Inc. All rights reserved.
doi:10.1016/j.yexcr.2004.04.015

elevation of intracellular Ca^{2+}, suggesting involvement of the $G_{q/11}$-phospholipase C pathway [11]. In contrast, we have shown $G_{q/11}$-induced apoptosis to be independent of protein kinase C activity and upregulation of intracellular Ca^{2+} in HeLa cells [8]. Other reports suggest an involvement of p38 mitogen-activated protein kinase and c-Jun N-terminal kinase activation in G_q-mediated cardiomyocyte apoptosis [3]. Thus, the molecular mechanisms of $G_{q/11}$-induced apoptosis are not clearly understood.

It has been recently established that several growth factors, including insulin and insulin-like growth factor, generate survival signals and prevent cell death. A central molecule in this context is Akt, which was first identified as the human homolog of a transforming oncogene [12]. Because Akt shares sequence similarity with protein kinase A and protein kinase C, it is also known as protein kinase B [13,14]. Regulation of Akt by G protein-coupled receptors has yet to be clarified. Initial work with fibroblasts provided evidence that lysophosphatidic acid, acting through $G_{i/o}$-coupled receptors, is unable to stimulate Akt [15]. Recent reports, however, indicate that Akt can be transiently activated in a variety of cells in response to ligands for G protein-coupled receptors such as thrombin [16], isoproterenol [17], *N*-formyl-Met-Leu-Phe, interleukin-8 [18], and carbachol [19]. Two contradictory papers on the regulation of Akt by G_q have been published: one reporting that a constitutively active mutant of G_q activates Akt in COS cells [19], and the other that the same mutant is unable to stimulate Akt but rather inhibits Akt stimulated with $G_{\beta\gamma}$, activated H-Ras, or insulin-like growth factor-1 in HEK293 cells and COS cells [20].

In the present study, we investigated the molecular mechanisms of $G_{q/11}$-induced apoptosis in HeLa cells and found that stimulation of $G_{q/11}$-coupled receptors can attenuate the activation of Akt by insulin and activate RhoA. The regulation of Akt by $G_{q/11}$ appears to be dependent on the activities of protein tyrosine phosphatase but independent of phospholipase C activity. These findings suggest the existence of a novel mechanism of $G_{q/11}$-induced apoptosis.

Materials and methods

Materials

pCMV5-FLAG-RhoAT19N and pCMV5-FLAG-RhoAG14V were generous gifts from H. Itoh (Nara Institute of Science and Technology), and pCMV-m1 receptor from E.M. Ross (University of Texas Southwestern Medical Center). pUSEamp-myc Akt (wild type), pUSEamp-myc Akt (activated), and pUSEamp-Bcl-2 were purchased from Upstate Biotechnology. pcDNA-3.1-3xhemagglutinin (HA)-tagged RGS2 was obtained from the Guthrie cDNA Resource Center (www.guthrie.org/AboutGuthrie/Research/cDNA). Rabbit polyclonal antibodies against $G\alpha_{q/11}$, insulin receptor substrate-1 (IRS-1), insulin receptor β, and mouse monoclonal antibody against RhoA were purchased from Santa Cruz Biotechnology. Rabbit polyclonal antibodies against Akt, phospho-Akt (Thr308), phospho-Akt (Ser473), and phospho-mitogen-activated protein kinase (MAPK), and mouse monoclonal antibody against phosphotyrosine-100 were purchased from Cell Signaling Technology. Mouse monoclonal antibodies against the HA epitope and ROCK-I were purchased from Roche Diagnostics and Transduction Laboratories, respectively. Mouse monoclonal antibodies against FLAG epitope and Hoechst 33342 were purchased from Sigma. Orthovanadate and okadaic acid were obtained from Wako. Y-27632, PD98059, wortmannin, and U-73122 were purchased from Calbiochem. To prepare pervanadate, sodium orthovanadate was prepared fresh in water at a concentration of 500 mM. Sodium orthovanadate (40 μl) and 5 μl of 30% (w/w) H_2O_2 were then added to 455 μl phosphate-buffered saline. This mixture was incubated for 5 min at room temperature before the addition of catalase (200 μg/ml) to remove the excess H_2O_2. The pervanadate solution was further incubated for 5 min at room temperature, immediately diluted in Dulbecco's modified essential medium (DMEM), and applied to cells [21].

Transfection, cell stimulation, and immunoblotting

HeLa cells were grown in DMEM supplemented with 10% fetal bovine serum at 37°C. Transient transfection with LipofectAMINE plus reagent was accomplished according to the manufacturer's instructions (Invitrogen). To examine the effect of m1 muscarinic stimuli on ROCK-I cleavage, HeLa cells were co-transfected with the m1 receptor and ROCK-I or other plasmids, cultured for 16 h in DMEM supplemented with 1× Insulin-Transferrin-Selenium-X supplement (Invitrogen), and stimulated with 100 μM carbachol. In some experiments, cells were incubated with 1 mM orthovanadate for 1 h before the addition of carbachol. To examine the effects of m1 muscarinic stimuli on the phosphorylation of Akt, HeLa cells were co-transfected with the m1 receptor and wild-type Akt or other plasmids, and cultured for 16 h in DMEM supplemented with 1× Insulin-Transferrin-Selenium-X supplement. Then the cells were washed twice with DMEM, incubated for 2 h in DMEM, and stimulated with 10 μg/ml insulin, 100 μM carbachol, or 10 μg/ml insulin plus 100 μM carbachol. In some experiments, cells were incubated for 1 h with 1 mM orthovanadate, for 10 min with 10 μM pervanadate, or for 30 min with 10 μM U-73122, 10 μM PD98059, and 10 μM Y-27632 before the addition of carbachol. Cells were lysed with 1% SDS in 20 mM Tris–HCl (pH 7.5), 1 mM EDTA, and lysates were subjected to SDS-polyacrylamide gel electrophoresis (PAGE) using 7.5% or 10% polyacrylamide gels for detection of ROCK-I, Akt, and other proteins. Immunoblotting was performed employing a chemiluminescence reagent (Perkin-Elmer Life Sciences), and densi-

tometry was achieved using the LAS-1000 system (Fujifilm) [8].

Immunoprecipitation

Transfected cells were washed twice with ice-cold phosphate-buffered saline and lysed with lysis buffer (20 mM Tris–HCl, pH 7.5, 1 mM EDTA, 1 mM EGTA, 5 mM $MgCl_2$, 25 mM NaF, 5 mM $Na_2S_2O_3$, 2 mM dithiothreitol, 0.2 mM Na_3VO_4, 0.1 μM calyculin A, 0.2 mM phenylmethanesulfonyl fluoride, 1 μg/ml of trypsin inhibitor) containing 1% Nonidet P-40 on ice for 20 min. Lysates were centrifuged at 10,000 × *g* for 10 min, and the supernatants were collected. Antibodies against insulin receptor β or IRS-I were added to the supernatants and incubated at 4°C for 2 h, followed by incubation with protein A-Sepharose for 1 h. The suspension was centrifuged at 1000 × *g* for 1 min, and the pellets were washed three times with 1 ml of lysis buffer containing 0.05% Nonidet P-40. Proteins bound to the beads were eluted in Laemmli sample buffer [22] and subjected to SDS-PAGE.

Apoptosis assay

Apoptotic measurements were carried out using a fluorometric method and counting cell numbers under as described previously [23]. This method involves the use of DNA-binding dyes Hoechst 33342 and propidium iodide. Hoechst 33342 is known to cross the plasma membrane of all cells, whether they are damaged or not, causing a blue fluorescence of their nuclei. The polar propidium iodide only penetrates cells with damaged membranes and leads to nuclear fluorescence. After treating cells for 4 h with various treatments, the cells were incubated with 5 μg/ml Hoechst 33342 and 5 μg/ml propidium iodide at 37°C, 5% CO_2 for 15 min. The medium was then removed by aspiration, and the cells were washed once with phosphate-buffered saline and then fixed by incubation with 4% paraformaldehyde for 30 min at room temperature. The percentage of apoptotic cells was counted by viewing cells under an inverted fluorescence microscope (Axiovert 200, Carl Zeiss) [23].

Extraction and measurement of 1,4,5-Inositol triphosphate

To examine the effect of U-73122 on m1-stimulated phospholipase C, cells were preincubated for 30 min with 10 μM U-73122 and exposed to 100 μM carbachol for 30 s. The reaction was stopped with 7.5% ice-cold trichloroacetic acid. The dishes were left on ice for 10 min, and the cells were scraped. The supernatants were centrifuged at 2000 × *g* for 15 min. The cell extracts were washed three times with 10 volumes of water-saturated diethyl ether and then titrated to pH 7.5 with 10% $NaHCO_3$ for assay. The level of 1,4,5-inositol triphosphate was determined by a competitive ligand-binding assay according to the manufacturer's instructions (Amersham Biosciences).

Pull-down assay for GTP-Rho

The GST-mDia fusion protein (residues −2 to 304) containing the Rho-binding domain (RBD) was expressed and purified as described previously [24]. Cells were lysed in 50 mM Tris–HCl (pH 7.5) containing 100 mM NaCl, 1 mM EDTA, 5 mM $MgCl_2$, 10% glycerol, 50 mM NaF, 1 mM Na_3VO_4, 1 mM dithiothreitol, 0.1% Nonidet P-40, 0.2 mM phenylmethanesulfonyl fluoride, and 1 μg/ml of trypsin inhibitor. The lysates were then subjected to centrifugation at 30,000 × *g* for 20 min at 4°C and the supernatants incubated with GST-RBD fusion protein conjugated with glutathione-coupled Sepharose 4B beads for 2 h at 4°C. The beads were washed three times with lysis buffer and subjected to SDS-PAGE. Bound RhoA was detected by immunoblotting with a monoclonal antibody against RhoA [24].

Other methods

Proteins were quantified using a microbicinchoninic acid protein assay kit (Pierce), with bovine serum albumin as the standard.

Results

To determine the signal pathway of $G_{q/11}$-mediated caspase activation in HeLa cells, we transfected cells with the $G_{q/11}$-coupled m1 receptor and examined how the agonist carbachol regulates caspase. Because ROCK-I is known to be cleaved by caspase 3 during G_{11}-induced apoptosis [8–10], we first determined the involvement of the mitochondrial apoptotic pathway. Carbachol-induced cleavage of ROCK-I was clearly reduced by expression of Bcl-2 (Fig. 1), which has the ability to exert a survival function in response to a wide range of apoptotic stimuli by blocking mitochondrial release of cytochrome *c* [25]. The same construct of Bcl-2 has been shown to prevent cell death in HN33 mouse hippocampal neuronal cells [26].

We next determine the involvement of Akt in $G_{q/11}$-induced caspase activation in HeLa cells. Expression of a constitutively active mutant of Akt inhibited the cleavage of ROCK-I by carbachol (Fig. 2), suggesting that $G_{q/11}$ negatively regulated the activity of Akt in HeLa cells. Previous report showed the same construct of Akt mutant to prevent fatty acid-induced apoptosis pancreatic β-cells [23]. Akt activation occurs by multiple phosphorylations on several residues [27]. Thr308 is located in the activation loop of kinase domain, and its phosphorylation by PDK1 is required for activation. The phosphorylation of Ser473 near the carboxyl-terminal region further potentiates activity [28]. Therefore, we monitored phosphorylation levels of Akt at Ser473 and Thr308 during carbachol stimulation by Western blot analysis using specific antibodies against phosphorylated Akt. As shown in Figs. 3A–C, detailed time course analyses revealed that carbachol markedly reduced phos-

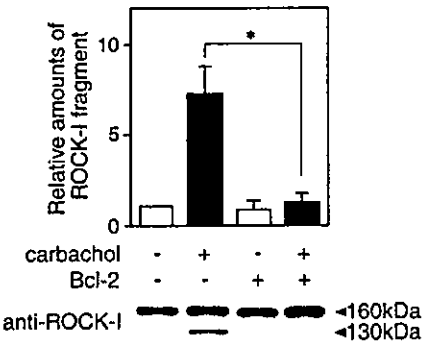

Fig. 1. Effect of Bcl-2 on carbachol-induced cleavage of ROCK-I in HeLa cells transfected with the m1 receptor. HeLa cells were co-transfected with the m1 receptor, ROCK-I and Bcl-2, and incubated in medium containing insulin for 16 h. Then cells were stimulated with 100 μM carbachol for 4 h, and lysates were immunoblotted with the antibody against ROCK-I. The intensity of the 130-kDa band (ROCK-I fragment) was quantified by densitometry and relative values are shown as means ± SD of data from four experiments (*$P < 0.01$).

phorylation levels at both Ser473 and Thr308, demonstrable as early as 5 min after agonist addition, with gradual reversal within 10 min, but remaining below control levels for 4 h. Although carbachol significantly reduced phosphorylation of Akt, its effect was weaker than that of wortmannin, a phosphoinositide 3-kinase inhibitor (Fig. 3D).

It is well-known that insulin signals are major survival signals in many cell systems that increase phosphorylation of Akt [29]. Treatment with carbachol almost completely inhibited insulin-stimulated phosphorylation of Akt at Ser473 (Fig. 4A, left panel), as well as at Thr308 (data not shown). In the same cell extracts, the phosphorylation of MAPK was stimulated by carbachol or insulin plus carbachol (Fig. 4A, right panel). The MEK inhibitor PD98059 reduced the stimulatory effect of carbachol on the phosphorylation of MAPK, but not the inhibitory effect of carbachol on insulin-stimulated Akt phosphorylation (Fig. 4A). These results indicated the pathway of $G_{q/11}$-regulated phosphorylation of Akt to be distinct from that of the $G_{q/11}$-stimulated MAPK cascade.

We have previously reported that G_{11}-mediated apoptosis does not involve protein kinase C activation and upregulation of intracellular Ca^{2+} through the products of phospholipase C activated by G_{11} [8]. However, it is still possible that the $G_{q/11}$-phospholipase C pathway mediates the induction of apoptosis due to the decrease of the substrate, phosphatidylinositol 4,5-bisphosphate, which is also a substrate for phosphoinositide 3-kinase. Such decrease may thus lower the quantity of the products formed by phosphoinositide 3-kinase, and consequently decrease the phosphorylation of Akt. The phospholipase C inhibitor U-73122 did not alter the effect of carbachol on insulin-stimulated Akt phosphorylation (Fig. 4B), whereas it inhibited phosphorylation of the $G\gamma_{12}$ subunit, which is mainly dependent on the phospholipase C-protein kinase C pathway [30]. To confirm the effect of U-73122 on phopholipase C further, we determined the production of 1,4,5-inositol phosphate in cells under the same conditions and found U-73122 to reduce the products in m1-stimulated cells (control, 1.72 ± 0.52 pmol/1 × 10^5 cells; carbachol, 10.97 ± 1.60 pmol/1 × 10^5 cells; U-73122 alone, 1.29 ± 0.57 pmol/1 × 10^5 cells; U-73122 plus carbachol, 5.72 ± 1.90 pmol/1 × 10^5 cells, $n = 4$). These results indicated that the effect of carbachol on Akt phosphorylation does not involve the $G_{q/11}$-phospholipase C pathway.

The decrease of Akt phosphorylation due to carbachol suggests the possible activation of serine–threonine protein phosphatases. However, the serine–threonine protein phosphatase inhibitor okadaic acid did not change the inhibitory effect of carbachol on insulin-stimulated phosphorylation of Akt (data not shown). It is well-known that insulin signaling is regulated by protein tyrosine kinases and phosphatases [31], and a recent report indicated $G_{q/11}$ to act on protein tyrosine phosphatase in HEK293 cells [32]. Treatment with tyrosine phosphatase inhibitors, orthovanadate (Fig. 4C, left) and pervanadate (Fig. 4C, right), partially blocked the effect of carbachol on insulin-stimulated Akt phosphorylation.

Insulin signals are dependent on the levels of tyrosine phosphorylation of the insulin receptor itself and related proteins [31]. We therefore examined the insulin receptor and IRS-1, which are hyperphosphorylated by insulin stimulation in many cells. The levels of tyrosine phosphorylation of IRS-1 were reduced by carbachol stimulation, but that of the insulin receptor did not significantly change (Figs. 5A and B). The change was blocked by orthovanadate, suggesting that $G_{q/11}$-activated protein tyrosine phosphatase acts on IRS-1 but not the insulin receptor.

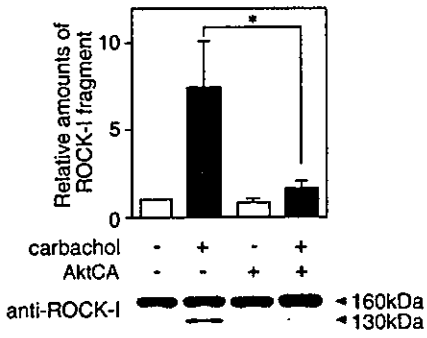

Fig. 2. Effect of a constitutively active form of Akt on carbachol-induced cleavage of ROCK-I in HeLa cells transfected with the m1 receptor. HeLa cells were co-transfected with the m1 receptor, ROCK-I and the constitutively active mutant of Akt (AktCA), and incubated in medium containing insulin for 16 h. Then cells were stimulated with carbachol for 4 h, and lysates were immunoblotted with the antibody against ROCK-I. The intensity of the 130-kDa band was quantified by densitometry and relative values are shown as means ± SD of data from four experiments (*$P < 0.01$).

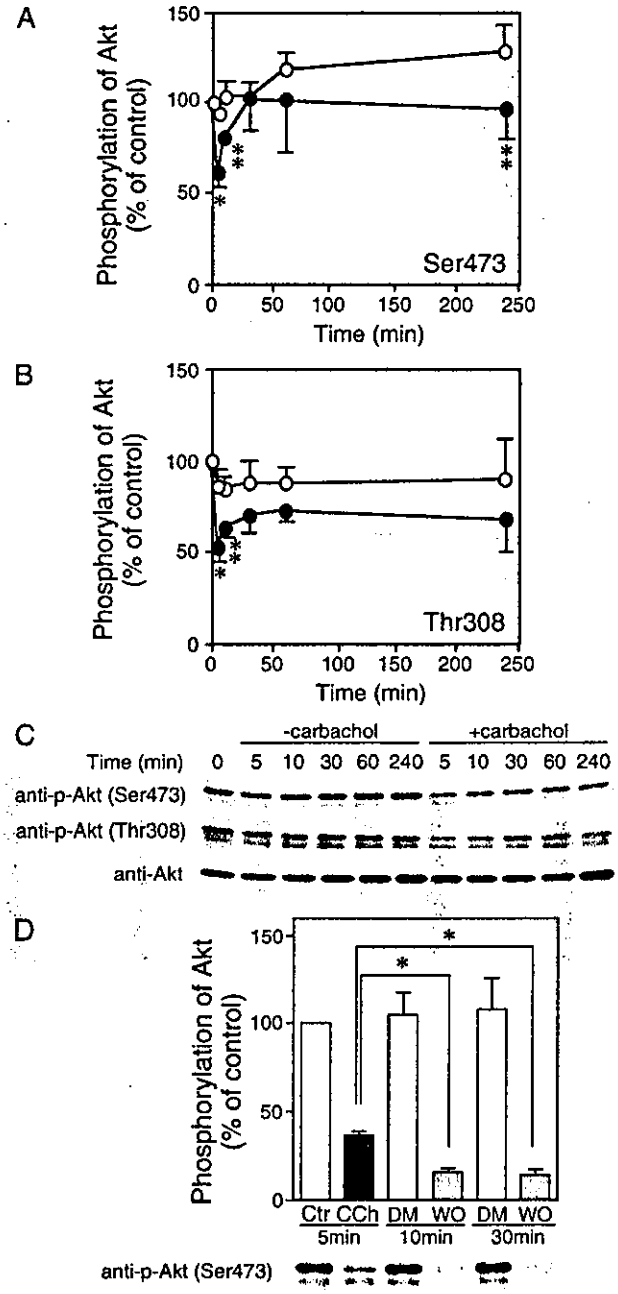

Fig. 3. Effect of carbachol on the phosphorylation of Akt. (A–C) Time course study. HeLa cells were co-transfected with the m1 receptor and wild type of Akt, and incubated in medium containing insulin for 16 h. Then cells were stimulated with carbachol for the indicated times, and lysates were immunoblotted with antibodies against phospho-Akt (Ser473), phospho-Akt (Thr308), and Akt (C). The intensities of phospho-Akt (Ser473) (A) and phospho-Akt (Thr308) (B) bands were quantified by densitometry and relative values are shown as means ± SD of data from four experiments. (○) Control, (●) Carbachol. $^{*}P < 0.01$, $^{**}P < 0.05$. (D) Comparison with the effect of wortmannin. Cells were incubated with 100 μM carbachol (CCh) for 5 min or with DMSO (DM) or 100 nM wortmannin (WO) for 10 or 30 min. The intensity of phospho-Akt (Ser473) bands was quantified by densitometry and relative values are shown as means ± SD of data from four experiments ($^{*}P < 0.01$).

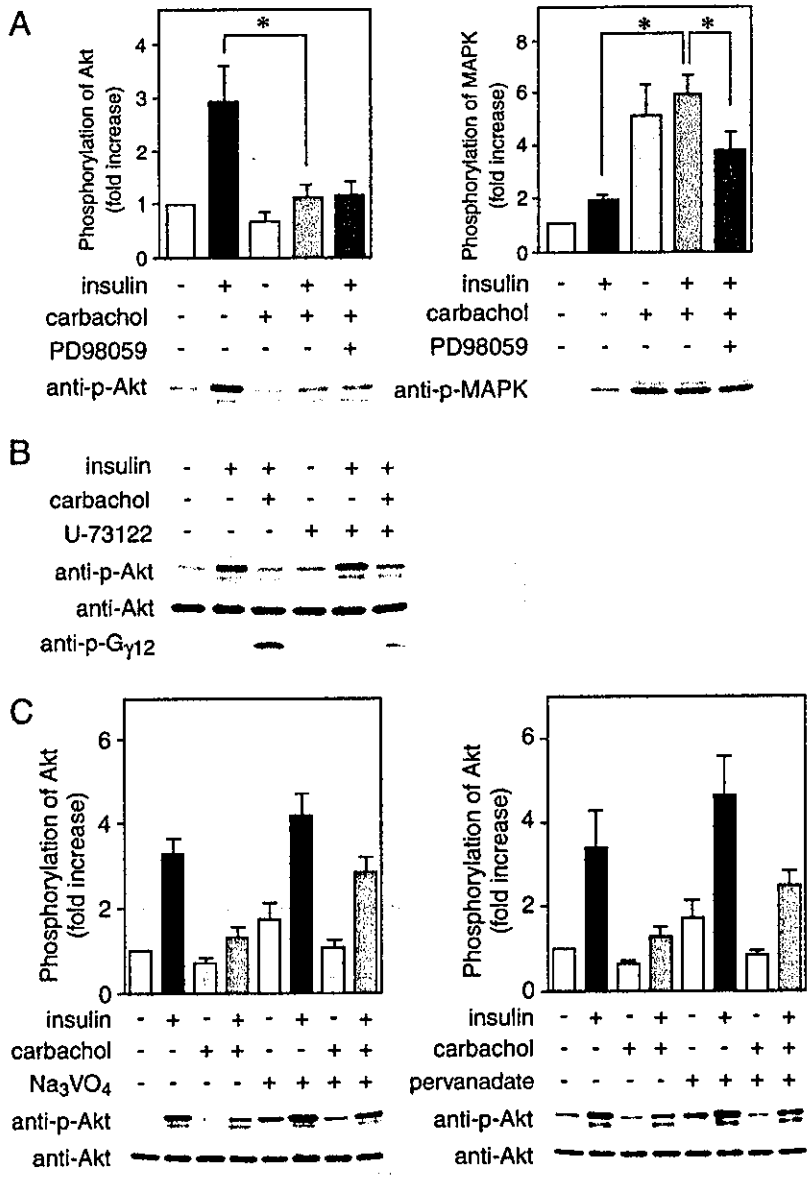

Fig. 4. Effects of carbachol on insulin-stimulated phosphorylation of Akt in the presence of inhibitors for MEK, phospholipase C, and protein tyrosine phosphatase. HeLa cells were co-transfected with the m1 receptor and wild-type Akt, incubated for 16 h, and starved in DMEM for 2 h. (A) Effects of an MEK inhibitor. Cells were stimulated with 10 μg/ml insulin, 100 μM carbachol, or 10 μg/ml insulin plus 100 μM carbachol for 5 min. In the combined case, they were incubated for 30 min with or without 10 μM PD98059 before the addition of carbachol. Cell lysates were immunoblotted with antibodies against phospho-Akt (Ser473) (left) and phospho-MAPK (right). The intensities of phospho-Akt (Ser473) and phospho-MAPK bands were quantified by densitometry and relative values are shown as means ± SD of data from four experiments. $^{*}P < 0.01$. (B) Effects of a phospholipase C inhibitor. Cells were stimulated with insulin or insulin plus carbachol for 5 min, either with or without prior treatment for 30 min with 10 μM U-73122, and lysates were immunoblotted with antibodies against phospho-Akt (Ser473), Akt, and phospho-$G\gamma_{12}$. (C) Effects of protein tyrosine phosphatase inhibitors. Cells were stimulated with insulin, carbachol, or insulin plus carbachol for 5 min, either with or without prior treatment for 1 h with 1 mM orthovanadate (left) and for 10 min with 10 μM pervanadate (right), and lysates were immunoblotted with antibodies against phospho-Akt (Ser473) and Akt. The intensity of phospho-Akt (Ser473) band was quantified by densitometry and relative values are shown as means ± SD of data from five experiments. Because tyrosine phosphatase inhibitors increased phosphorylation of Akt in all cases, it seems to be difficult to directly compare with that in the absence of inhibitors. The ratios of the phosphorylation with insulin plus carbachol to that with insulin alone were obtained as follows (means of five experiments): without orthovanadate, 0.34; with orthovanadate, 0.66; without pervanadate, 0.37; with pervanadate, 0.55. These values show the partial blockage of the carbachol effect by tyrosine phosphatase inhibitors.

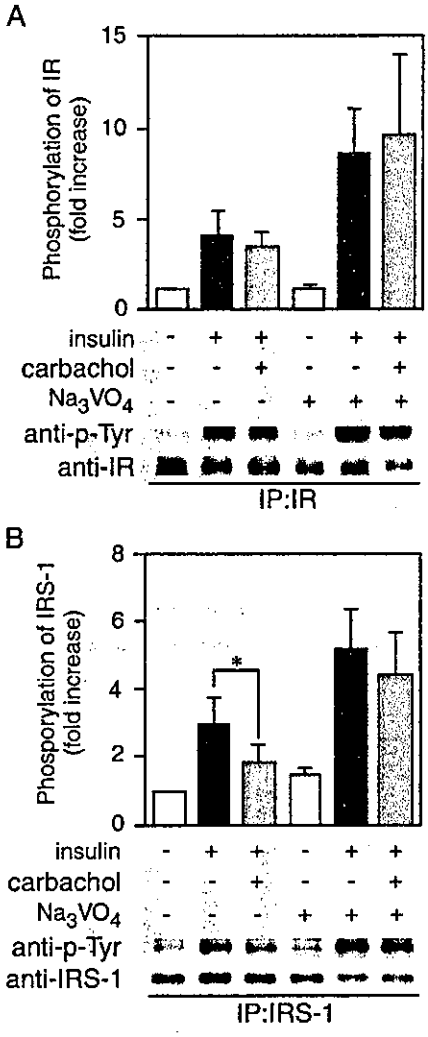

Fig. 5. Effects of carbachol on insulin-stimulated tyrosine phosphorylation of the insulin receptor and IRS-1 in the presence or absence of orthovanadate. HeLa cells were transfected with the m1 receptor, incubated for 16 h, and starved in DMEM for 2 h. Then they were stimulated with insulin, carbachol, or insulin plus carbachol for 5 min, either with or without prior treatment for 1 h with 1 mM orthovanadate. Cell lysates were subjected to immunoprecipitation with antibodies against the insulin receptor (IR) (A) and IRS-1 (B). Then immunoprecipitates were immunoblotted with antibodies against phosphotyrosine (p-Tyr), the insulin receptor (A), and IRS-1 (B). The intensities of tyrosine phosphate in the insulin receptor and IRS-1 bands were quantified by densitometry. Because the expression of the insulin receptor and IRS-1 was decreased by treatment of orthovanadate, ratios of tyrosine phosphorylation (p-Tyr/IR or p-Tyr/IRS-1) were obtained. Relative values are shown as means ± SD of data from five experiments (*$P < 0.01$).

Because the effect of carbachol to inhibit insulin-stimulated Akt phosphorylation was only partially eliminated by orthovanadate or pervanadate, we expected a contribution of at least one more pathway underlying carbachol-regulated Akt phosphorylation. Recent reports of G_q and m1 stimulation activating RhoA [33,34] lead us to examine whether this pathway is involved. To determine whether carbachol activates RhoA in HeLa cells, we measured the activation of endogenous RhoA by pull-down method using GST-mDia-RBD. A time course analysis revealed the rapid and potent activation of RhoA, which was demonstrable as soon as 1 min after carbachol addition and was attenuated within 10 min (Fig. 6).

To test whether these effects of carbachol were indeed mediated by $G_{q/11}$, we co-expressed the m1 receptor and RGS2, a $G\alpha_{q/11}$-specific GTPase-activating protein, which is expected to bind and sequester $G_{q/11}$ [35]. Expression of RGS2 eliminated the effects of carbachol on insulin-induced Akt phosphorylation (Fig. 7A) and on RhoA activity (Fig. 7B). Previous report showed that the same construct of RGS2 blocked m1-mediated serum response factor activation [36].

Next we studied whether expression of dominant-negative and constitutively active mutants of RhoA influences ROCK-I cleavage. We have previously shown that the same construct of the dominant-negative mutant completely inhibited Gβγ-induced stress fiber formation in HeLa cells [37], and that of the constitutively active form inhibited lysophosphatidic acid-induced spreading of NIH3T3 cells [38]. The constitutively active mutant of RhoA strongly induced ROCK-I cleavage, which was not further increased by carbachol stimulation (Fig. 8A). On the other hand, the dominant-negative mutant of RhoA inhibited carbachol-induced ROCK-I cleavage, though this mutant alone slightly

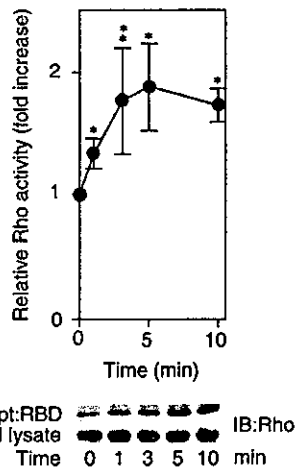

Fig. 6. Carbachol-induced activation of endogenous RhoA. HeLa cells were transfected with the m1 receptor, incubated for 16 h, and starved in DMEM for 2 h. Then the cells were stimulated with carbachol for the indicated times. Cell lysates were subjected to the pull-down assay with GST-mDia-RBD, and precipitated RhoA and cell lysates were immunoblotted with the antibody against RhoA. The intensity of RhoA band in each precipitate was quantified by densitometry, and relative values are shown as means ± SD of data from five experiments (*$P < 0.01$, **$P < 0.05$).